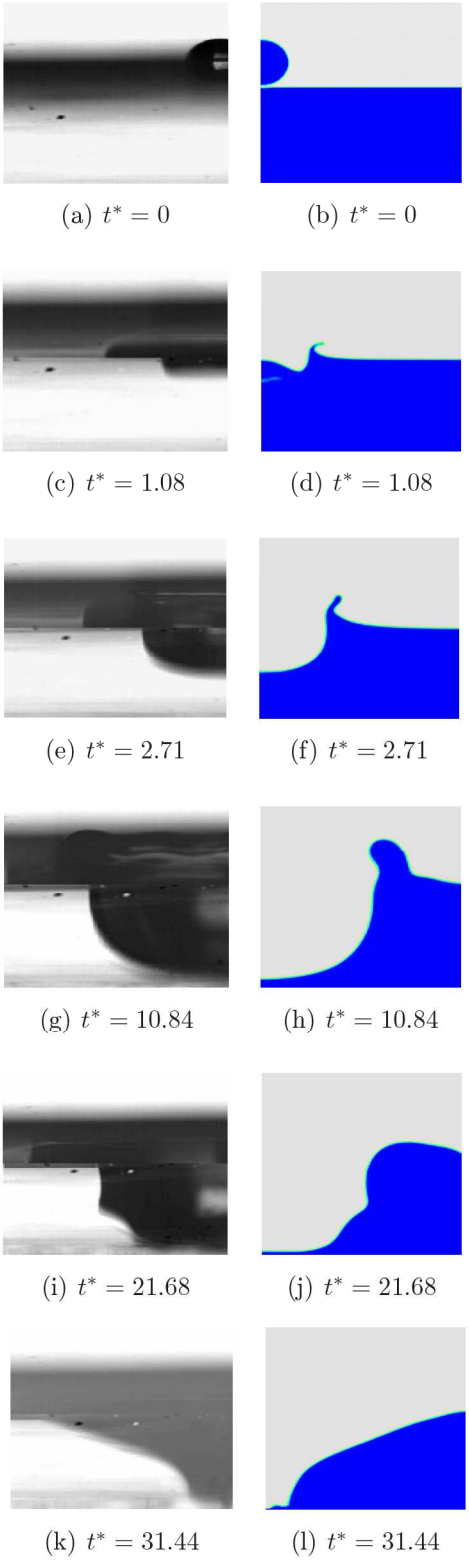

(a) $t^* = 0$ (b) $t^* = 0$

(c) $t^* = 1.08$ (d) $t^* = 1.08$

(e) $t^* = 2.71$ (f) $t^* = 2.71$

(g) $t^* = 10.84$ (h) $t^* = 10.84$

(i) $t^* = 21.68$ (j) $t^* = 21.68$

(k) $t^* = 31.44$ (l) $t^* = 31.44$

Figure 4.10: Single drop impingement onto a liquid layer of non-dimensional thickness $h^* = 2$: (left) experiments and (right) numerical simulations (Beberovic *et. al.* [10]). The evolution of the cavity formed by an isopropanol drop ($We = 392$, $Fr = 257$, $Re = 1,733$) impingement at various non-dimensional time instants

hemispherical to conical, see Figures 4.9(j) and 4.9(l) for distilled water and Figures 4.10(j) and 4.10(l) for isopropanol. At the receding phase, capillary waves travel downwards along the surface of the cavity. At the moment that the capillary waves merge at the bottom of the cavity, this leads to a sharp bottom of the cavity, where high pressure differences and surface tension forces are present, due to which the cavity retracts from the bottom of the liquid film and forms a central jet, Figure 4.1.

In this paragraph the drop impingement process, in particular the dynamics of the cavity that appears below the liquid surface film upon drop impingement, has been described and analysed in a detailed qualitative way. Drop impingement is characterised by several typical time and length scales, among others the depths and diameters of the cavities and the times at which the maximum values of these length scales are reached. To determine quantitatively the influence of the different drop and film parameters, which have been described above, on the impingement process, the next paragraphs focus on the time evolution of these typical length scales.

4.2 Evolution of the diameter of the cavity in time

This paragraph presents the detailed results of the diameter evolution of the cavity in time upon impingement of a single drop onto a steady liquid film of finite thickness. The diameter of the cavity is determined at a depth of 50% of the initial film thickness, hence, $y_{cav}/h^* = 0.5$, where y_{cav} is the vertical distance measured from the free surface of the liquid film. For the analysis of the numerical simulations shown hereafter, the diameter is determined using the computational cells where the volume fraction becomes $\gamma \geq 0.5$. The results of the experiments are compared with the analytical models and numerical simulations to validate the theoretical models and the numerical code. Several particular impingements of the many impingement experiments conducted are selected and presented in more detail hereafter. The impingement parameters of all the experiments, together with the inputs for the analytical models, are listed in Table 4.2.

4.2.1 Theoretical analysis of the cavity radius evolution: propagation of a kinematic discontinuity

One of the significant results of the experimental and theoretical study conducted by Yarin and Weiss [196] is the theoretical model of a flow generated by drop impingement and the emergence of the uprising liquid sheet. A remote asymptotic solution for the film flow in the liquid layer is obtained in non-dimensional form:

$$h^*_{film} = \frac{A}{(t^* - \tau_{fit})^2} \tag{4.1}$$

$$u^*_{r,film} = \frac{R^*_{cav}}{t^* - \tau_{fit}} \tag{4.2}$$

Here h^* is the non-dimensional film thickness, t^* the non-dimensional time after impingement, τ_{fit} the non-dimensional time-shift needed for curve-fitting, R^*_{cav} the non-dimensional radius of the cavity and u^*_r the non-dimensional radial film velocity, whereas A is a constant. To make the variables non-dimensional, the initial drop diameter is used as a length scale and the

Table 4.2: Parameters of the conducted experiments used for discussion of the impingement outcomes and comparison with analytical models and numerical simulations

Liquid	h^*	We	Fr	Re	$D^*_{cav,max}$	$t^*_{cav,max}$	$t^*_{retraction}$	β	τ
Distilled water	0.5	111	99	4,871	3.07	6.2	13.1	0.93	0.50
Distilled water	0.5	238	207	7,173	3.86	9.3	20.4	0.77	0.50
Distilled water	0.5	332	299	8,392	4.39	11.9	28.5	0.75	0.50
Distilled water	1.0	105	94	4,744	2.98	8.4	12.9	0.74	0.94
Distilled water	1.0	239	202	7,241	3.83	13.1	22.4	0.61	0.94
Distilled water	1.0	328	296	8,342	4.54	15.7	31.1	0.60	0.94
Distilled water	1.5	110	95	4,870	2.55	6.2	12.6	0.60	1.30
Distilled water	1.5	232	199	4,115	3.31	11.4	21.6	0.52	1.30
Distilled water	1.5	341	296	8,587	3.97	17.2	30.3	0.51	1.30
Distilled water	2.0	113	98	4,948	2.39	6.7	11.9	0.55	1.70
Distilled water	2.0	215	194	6,750	3.13	10.9	21.1	0.50	1.70
Distilled water	2.0	345	294	8,644	3.84	15.5	29.8	0.48	0.70
Isopropanol	0.5	194	132	1,208	3.85	9.0	18.3	0.85	0.50
Isopropanol	0.5	384	261	1,701	4.50	15.4	31.8	0.74	0.50
Isopropanol	0.5	541	375	2,007	4.90	21.7	41.6	0.73	0.50
Isopropanol	1.0	192	131	1,201	3.50	8.5	18.5	0.64	0.94
Isopropanol	1.0	384	261	1,701	4.76	19.2	33.2	0.60	0.94
Isopropanol	1.0	539	367	2,013	4.91	20.2	44.9	0.53	0.94
Isopropanol	1.5	192	128	1,206	3.11	9.8	17.9	0.54	1.30
Isopropanol	1.5	392	257	1,733	4.27	18.2	31.8	0.51	1.30
Isopropanol	1.5	535	365	2,006	4.65	21.7	42.9	0.48	1.30
Isopropanol	2.0	189	127	1,199	2.92	10.1	18.3	0.54	1.70
Isopropanol	2.0	392	257	1,733	4.03	19.1	31.8	0.50	1.70
Isopropanol	2.0	527	366	1,982	4.32	21.8	41.6	0.46	1.70
Glycerine/Water	0.5	151	128	299	2.96	6.0	15.5	0.76	0.50
Glycerine/Water	0.5	318	258	444	3.99	12.0	26.5	0.68	0.50
Glycerine/Water	0.5	472	383	539	4.12	16.7	36.7	0.59	0.50
Glycerine/Water	1.0	162	130	341	2.70	7.1	15.4	0.55	0.94
Glycerine/Water	1.0	329	260	428	3.74	12.6	27.6	0.52	0.94
Glycerine/Water	1.0	465	384	526	4.53	21.7	39.1	0.51	0.94
Glycerine/Water	1.5	156	129	317	2.69	7.2	15.2	0.52	1.30
Glycerine/Water	1.5	328	260	447	3.48	13.7	27.3	0.45	1.30
Glycerine/Water	1.5	473	378	529	4.20	19.9	38.4	0.44	1.30
Glycerine/Water	2.0	157	128	320	2.45	7.4	14.5	0.47	1.70
Glycerine/Water	2.0	308	254	434	3.35	14.8	27.2	0.44	1.70
Glycerine/Water	2.0	505	399	561	3.83	19.3	38.8	0.40	1.70

impingement velocity as the velocity scale. The radially expanding flow generated by drop impingement onto a dry wall (Roisman *et al.* [136]) or the velocity field in the inner region of the flow generated by drop impingement onto a liquid film (Roisman and Tropea [138] and [137]) can be described very well by the equations (4.1) and (4.2).

The dynamics of the motion of the crown base can be described theoretically by approximating it as a propagation of a kinematic discontinuity in the liquid film (Yarin and Weiss [196]). The expression for the non-dimensional radius of the crown and thus of the upper part of the cavity R_{cav} can be obtained in the form:

$$R^*_{cav} = \sqrt{\beta(t^* - \tau)} \tag{4.3}$$

Here β is a constant. This constant is determined by the initial phase of the drop deformation at impingement and by the drop penetration in the liquid film. Generally it also depends on the Reynolds number and Weber number, as well as on the non-dimensional initial film thickness. In the case of inertia dominated drop impingement, however, the effects of the viscosity and surface tension are negligibly small and the parameter β is determined solely by the initial thickness of the undisturbed liquid film (Yarin and Weiss [196]).

In the theoretical study by Trujillo and Lee [173] the effect of the viscosity on the propagation of the kinematic discontinuity is taken into account. It is shown that if the Reynolds number and Weber number of the impinging drop are high enough, the influence of the viscosity on R^*_{cav} is negligibly small. In Roisman and Tropea [137] the theory of Yarin and Weiss is generalized for non-axisymmetric drop impingements, like oblique impingement, impingement onto a moving film or the interaction of two impinging drops. They have obtained an analytical solution for the crown shape.

The classical expression (eq. (4.3)) for the development of the cavity radius with time is supported by numerous experimental data (Cossali *et al.* [26]) and by the results of numerical simulations of the drop impingement process (Rieber and Frohn [129]). The equations (4.1) and (4.2) describe well the film thickness created by a drop impinging onto a dry spherical target (Bakshi *et al.* [7]), since for these cases the liquid surface film is thicker then the viscous boundary layer.

It has been observed by Sivakumar and Tropea [156], however, that for drop impingement onto a liquid layer formed by spray impingement, the cavity diameter reaches a maximum and even starts to reduce due to the influence of the surface tension forces acting on the cavity. Such behavior cannot be described by eq. (4.3). They show, that the deviation from the square-root law, given by eq. (4.3), is attributed to the crown-crown interaction during the spray impingement process. For the experimental data, presented hereafter, the diameter evolution of the cavity/crown, produced by a single drop impingement onto a liquid layer of finite thickness, also deviates from the $t^{1/2}$-law. This deviation can thus be explained only by the influence of surface tension and gravity, which is not accounted for in the derivation of eq. (4.3).

Governing equations

If the drop impingement velocity is high enough, the Reynolds number and Weber number are much higher than unity, resulting in a flow associated with the cavity expansion, that is governed mainly by inertia, surface tension and gravity. The expansion of the cavity is described by the propagation of a kinematic discontinuity (Yarin and Weiss [196]) that divides the liquid surface film into the inner region of thickness $h(r,t)$ and the outer stationary undisturbed

surface film of constant thickness h^*.

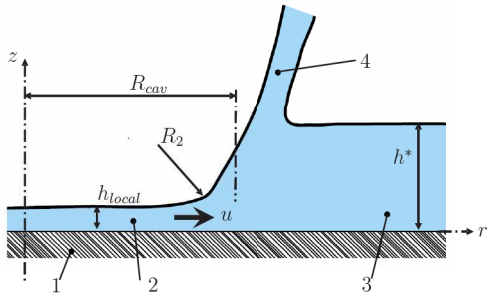

Figure 4.11: Sketch of a kinematic discontinuity propagating towards the liquid layer: 1 is the target surface, 2 the inner region of the liquid surface film, 3 the outer static undisturbed region of the liquid surface film and 4 the uprising crown-like sheet

The average velocity through the film cross-section is denoted $u(r,t)$. A sketch of the propagating kinematic discontinuity is shown in Figure 4.11.

It can be shown that the remote asymptotic solution, given by eq. (4.1) and eq. (4.2), exactly satisfies the mass and the momentum balance equations for the inviscid flow, even if the capillary forces and gravity are significant. The propagation velocity of the kinematic discontinuity can be found by applying the quasi-stationary Bernoulli equation (Roisman and Tropea [137]). Here, this equation is modified accounting for the average pressure drop associated with gravity and surface tension, denoted respectively as:

$$p_g \approx \frac{\rho g(h - h_{local})}{2} \tag{4.4}$$

$$p_\sigma \approx -\sigma\left(\frac{1}{R_{cav}} + \frac{1}{R_2}\right) \tag{4.5}$$

Here R_2 is the curvature of the film profile, whereas R_{cav} is the radius of the cavity at $z = h/2$. The expression for the capillary pressure is obtained from the Young-Laplace relation, describing the correlation between the surface tension, pressure and curvature of the surface. In this expression, the last term within the brackets is the approximate expression for the total curvature of a surface of rotation. The Bernoulli equation yields the following equation for the velocity U_{cav} of the propagation of the kinematic discontinuity:

$$\frac{\rho(u - U_{cav})^2}{2} + p_\sigma = \frac{\rho U_{cav}^2}{2} + p_g \tag{4.6}$$

In the derivation of this equation the pressure drop due to the viscous drag is neglected. This assumption is valid only for the very high impingement Reynolds numbers leading to the cavity formation and typical of the experiments described hereafter. At such high Reynolds numbers the viscosity effect is significant only at relatively thin boundary layers. The viscous dissipation in these layers leads to the thickening of the boundary layer, but it cannot influence the outer solution and thus does not effect the crown propagation.

The solution of the Bernoulli equation (eq. (4.6)), hence, the velocity with which the cavity surface is moving in time, can be written as:

$$U_{cav} = \frac{u}{2} - g\frac{h - h_{local}}{2u} - \left(\frac{1}{R_2} + \frac{1}{R_{cav}}\right)\frac{\sigma}{\rho u} \tag{4.7}$$

Equation (4.7) can be written in non-dimensional form and simplified, accounting for the fact that at large times after impingement $h^*_{local} \ll h^*$:

$$U^*_{cav} = \frac{dR^*_{cav}}{dt^*} = \frac{u^*}{2} - \frac{h^*}{2u^*Fr} - \left(\frac{1}{R^*_2} + \frac{1}{R^*_{cav}}\right)\frac{1}{u^*We} \tag{4.8}$$

The variables in this equation are written in non-dimensional form using the initial drop diameter as a length scale and the impingement velocity as a velocity scale. This is an ordinary differential equation for the propagation of the cavity radius in time $R^*_{cav}(t^*)$, which can be solved numerically with the help of equations (4.1) and (4.2), when the value of R^*_2 is known. From geometrical considerations (see the sketch in Figure 4.11) it is assumed that R^*_2 is comparable with the initial surface film thickness h^*. In the present model the value for R^*_2 is set to $R^*_2 = h^*/2$. This assumption is based on the fitting of the model predictions to the experimental data, presented in §(4.2.2). It can be shown that in the case of $We \to \infty$ and $Fr \to \infty$ eq. (4.8) has an analytical solution in the asymptotic form given by eq. (4.3) obtained by Yarin and Weiss [196].

Asymptotic solution for maximum cavity radius at We $\gg$ 1 and Fr $\gg$ 1

In this paragraph drop impingements with finite, but large values of the impingement Weber number and Froude number are considered. In this case the terms corresponding to gravity and surface tension become significant only at the late stages of the cavity spreading period. The cavity radius deviates from the asymptotic square-root behavior (eq. (4.1) and eq. (4.2)), when the velocity of the inner region is small enough, hence: $u \sim Fr^{-1/2}$ or $u \sim We^{-1/2}$. The cavity radius at this stage is comparable with the maximum cavity radius $R^*_{cav,max}$. Accounting for the small values of the terms involving $1/Fr$ and $1/We$ eq. (4.8) can be simplified to the following form:

$$U^*_{cav} = \frac{dR^*_{cav}}{dt^*} \approx \frac{u^*}{2} - \frac{h^*}{2u^*Fr} - \left(\frac{2}{h^*} + \frac{1}{R^*_{cav,max}}\right)\frac{1}{u^*We} \tag{4.9}$$

The solution of this equation is given as:

$$R^*_{cav} = \sqrt{\beta T^* - \left(\frac{2h^*}{R^{*2}_{cav,max}We} + \frac{4}{We} + \frac{h^{*2}}{Fr}\right)\frac{T^{*2}}{h^*}} \tag{4.10}$$

$$T^* = t^* - \tau \tag{4.11}$$

Here β is defined as a constant, see eq. (4.3). The instant $T^*_{cav,max}$ at which the radius of the expanding cavity reaches its maximum value can therefore be expressed in the form:

$$T^*_{cav,max} = \frac{\beta h^*}{2}\left(\frac{2h^*}{R^{*2}_{cav,max}We} + \frac{4}{We} + \frac{h^{*2}}{Fr}\right)^{-1} \tag{4.12}$$

The value of the maximum cavity radius can now be obtained as the positive real root of the equation:

$$R^*_{cav}(T^* = T^*_{cav,max}) = R^*_{cav,max} \tag{4.13}$$

which, with the help of eq. (4.10) and accounting for the large values of We and Fr, yields:

$$R^*_{cav,max} = \frac{\beta\sqrt{h^*}}{2\sqrt{G}} - \frac{h^*}{GWe} \tag{4.14}$$

$$G = \frac{4}{We} + \frac{h^{*2}}{Fr} \tag{4.15}$$

The value of the parameter τ is by definition independent of the Weber number and Froude number, hence, it is only a function of the initial surface film thickness, $\tau = \tau(h^*)$, whereas β is a function of the Reynolds number and the initial film thickness, $\beta = \beta(Re, h^*)$.

4.2.2 Results: dynamics of the diameter of the cavity in time

Evaluation of the analytical models

In order to compare the experimental results of the time evolution of the diameter of the cavity, measured at $y_{cav}/h^* = 0.5$, with the analytical model for the time evolution of the cavity diameter, derived in §(4.2.1) and described by eq. (4.10), it is important to evaluate this theoretical model before. This evaluation is done by looking at two important scaling parameters that are relevant to spray impingement modeling: the magnitude of the maximum cavity diameter $D^*_{cav,max.}$ and the non-dimensional time at which this maximum cavity diameter is reached $t^*_{cav,max.}$. By comparing the experimentally obtained maximum diameter of the cavity and the non-dimensional time at which this maximum cavity diameter is reached with, respectively, the analytical solutions given by eq. (4.14) and (4.12) it can be tested whether this theoretical model can be used to predict the time evolution of the cavity diameter.

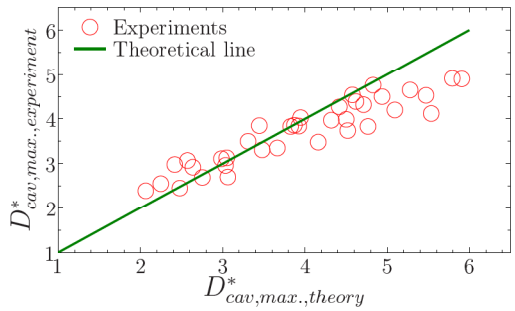

(a) Comparison maximum cavity diameter

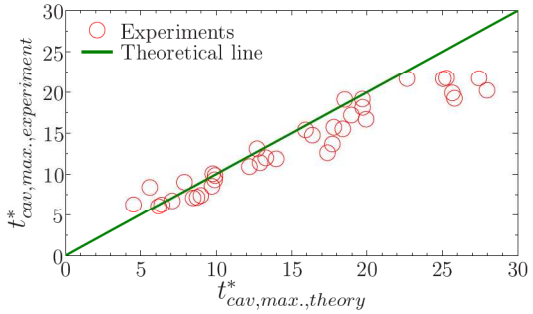

(b) Comparison time of maximum cavity diameter

Figure 4.12: Comparison of the theoretical predictions of the maximum diameter of the cavity and the non-dimensional time at which the maximum cavity diameter is reached with the experimental data. The impingement parameters and the inputs for the analytical model are listed in Table 4.2

In the Figures 4.12(a) and 4.12(b) the theoretical predictions of the maximum cavity diameters and the non-dimensional times for the maximum cavity diameters are compared with the experimentally obtained data. In each figure all the conducted experiments listed in Table 4.2 are taken into account. Both figures show a rather good agreement between the experiments and the analytical solutions for most of the experiments, indicating that the assumptions taken in the derivation of the theory, see §(4.2.1), are valid. Only for very high maximum

non-dimensional diameters of the cavities and non-dimensional times of maximum cavity a discrepancy up to 30% is seen to occur. Several adjustable parameters are used in this model, hence R_2, τ and β. The values of the parameters τ and β are listed for all the experiments in Table 4.2 and plotted in the Figures 4.13(a) and 4.13(b).

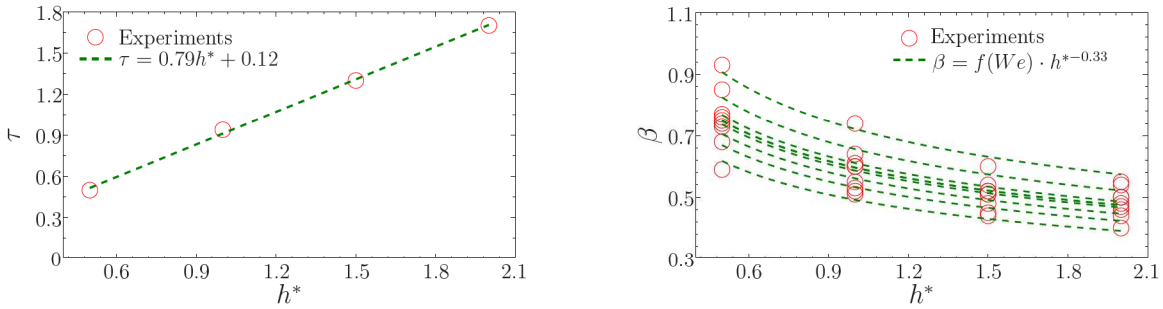

(a) Parameter τ (b) Parameter β

Figure 4.13: Fitted values of the parameters τ and β as a function of the non-dimensional initial liquid film thickness and Weber number. The exact values for β are listed in Table 4.2

As was mentioned already in the derivation of the equations for the diameter evolution it is assumed that the values for τ depend only on the initial liquid film thickness h^*, whereas the values for β are a function of the initial film thickness and the Weber number of the impinging drop. The values for τ and β are obtained by fitting the analytical solution (eq. (4.10)) with the experimental data. The magnitudes of the parameters τ and β can be best expressed in the following forms:

$$\tau = 0.79h^* + 0.12, \qquad 0.5 \leq h^* \leq 2 \tag{4.16}$$

$$\beta = f(We) \cdot h^{*-0.33}, \qquad 0.5 \leq h^* \leq 2 \tag{4.17}$$

The results shown above clearly indicate that this model can be used to predict in good agreement the time evolution of the cavity diameter for all conducted measurements. In the following discussion the experimentally obtained results for the cavity diameter, together with the numerical simulations and the analytical model, will be presented to describe the influence of the initial film thickness, Weber number and liquid properties on the time evolution of the cavity diameter. In these paragraphs the impingement process is split up into two parts: the initial phase of drop impingement and the complete impingement process. The initial impingement stage spans a non-dimensional time range between $t^* = 0$ and $t^* \approx 12$ and is used to evaluate the models, that describe the initial diameter change. In the paragraph thereafter the complete drop impingement process will be evaluated, in which the experimental data of the diameter evolution of the cavity in time will be compared with the analytical models and the numerical simulations.

Initial phase of drop impingement

Figure 4.14 shows a comparison between the measured evolution of the diameter of the cavity at the initial stage of drop impingement and the analytical model given by eq. (4.3). Figures 4.14(a) and 4.14(b) show the change of the cavity diameter squared for three different

drop Weber numbers for $h^* = 0.5$ and $h^* = 1.0$ respectively for isopropanol, whereas in Figure 4.14(c) the evolution of the cavity diameter squared for distilled water ($h^* = 1.0$) for three different Weber numbers is presented. A detailed comparison for all the investigated initial film thicknesses and liquids can be found in Appendix A.

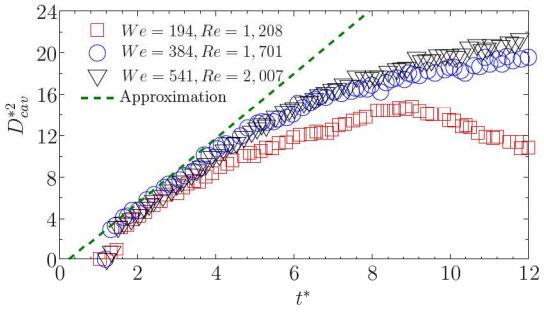

(a) Isopropanol, $h^* = 0.5$

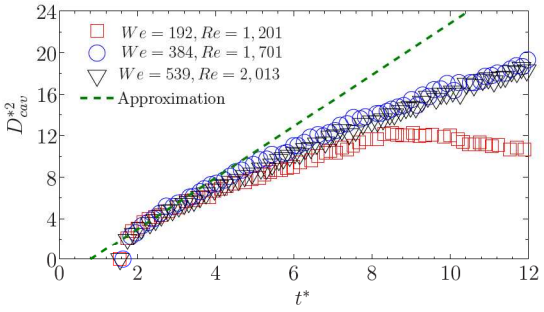

(b) Isopropanol, $h^* = 1.0$

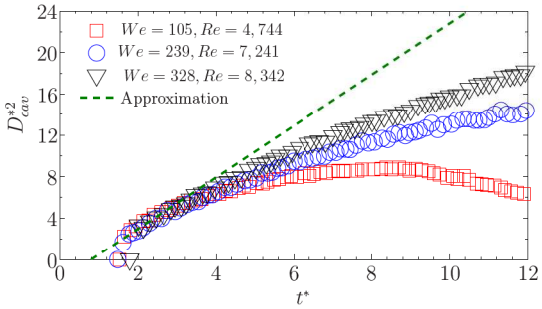

(c) Distilled water, $h^* = 1.0$

Figure 4.14: Comparison of the experimental results with the analytical solution (eq. (4.3), Yarin and Weiss [196]) of the diameters of the cavity for various experiments at the initial stage of the cavity expansion. The square of the diameter D^*_{cav} is shown as a function of the non-dimensional time t^*. The impingement parameters for the experimental data are listed in Table 4.2

At the initial stage after impingement, hence $1 \leq t^* \leq 6$, the values of D^{*2}_{cav} increase linearly with time, therefore confirming the theoretical predictions given by eq. (4.3). This means that the remote asymptotic solution, developed by Yarin and Weiss [196] for non-dimensional times $t^* \gg 1$, can also be used to describe the expansion of the cavity diameter for the initial impingement phase. For non-dimensional times $t^* > 6$ an increasing deviation from the analytical solution can be seen for the change of the cavity diameter with time. For lower Weber and Froude numbers this deviation begins at smaller non-dimensional times and increases faster. To predict the expansion of the diameter of the cavity precisely for larger times after impingement a model has to be applied that also accounts for the influence of surface tension and gravity. This model has been derived in §(4.2.1) and is given by eq. (4.10).

Later stages of drop impingement

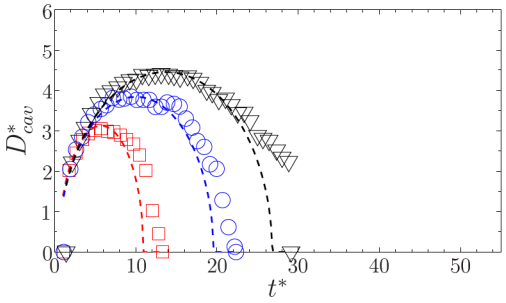

(a) Distilled water; □: $h^* = 0.5$, $We = 111$, $Re = 4,871$; ◯: $h^* = 0.5$, $We = 238$, $Re = 7,173$; ▽: $h^* = 0.5$, $We = 332$, $Re = 8,392$

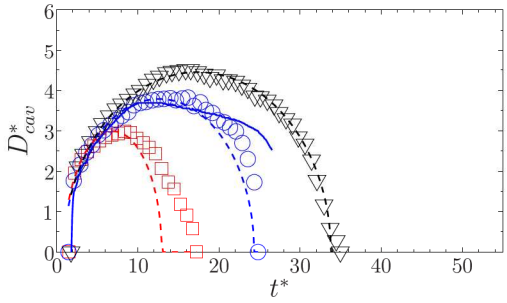

(b) Distilled water; □: $h^* = 1.0$, $We = 105$, $Re = 4,744$; ◯: $h^* = 1.0$, $We = 239$, $Re = 7,241$; ▽: $h^* = 1.0$, $We = 328$, $Re = 8,342$

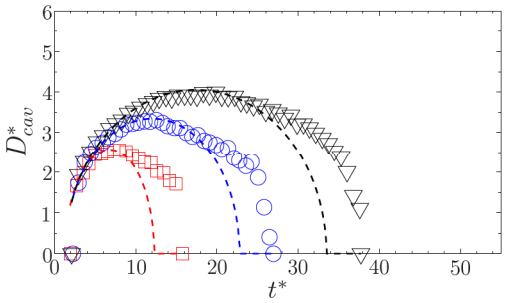

(c) Distilled water; □: $h^* = 1.5$, $We = 110$, $Re = 4,870$; ◯: $h^* = 1.5$, $We = 232$, $Re = 7,115$; ▽: $h^* = 1.5$, $We = 341$, $Re = 8,587$

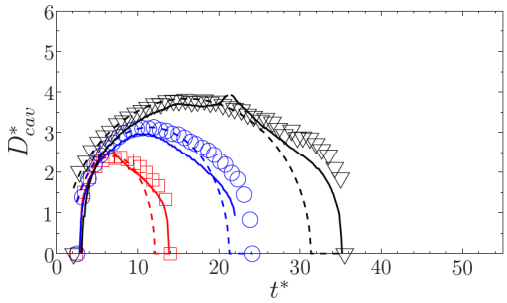

(d) Distilled water; □: $h^* = 2.0$, $We = 113$, $Re = 4,948$; ◯: $h^* = 2.0$, $We = 215$, $Re = 6,750$; ▽: $h^* = 2.0$, $We = 343$, $Re = 8,644$

Figure 4.15: Evolution of the diameter of the cavity in time, measured at $y/h^*_{cav} = 0.5$, for different initial film thicknesses. Comparison of the experimental results (□, ◯, ▽) with the theoretical predictions (eq. (4.10), dashed line) and the numerical simulations (solid line) for distilled water. The impingement parameters for the experimental data and the inputs for the analytical model are listed in Table 4.2

Plots of the non-dimensional cavity diameter D^*_{cav} against the non-dimensional time t^* for the four investigated initial liquid film thicknesses are given in Figure 4.15 for distilled water, in Figure B.5 for isopropanol and in Figure B.6 for the glycerine/water mixture. The symbols in the figures correspond to the experimental data, the solid lines are the numerical simulations and the dashed lines the theoretical results (eq. (4.10)). The corresponding values of the parameters τ and β are listed in Table 4.2.

In general it can be said that the curves for the cavity diameters all have a parabolic shape, which can be split up into the expansion phase of the cavity (for $0 \leq t^* \leq t^*_{cav,max.}$) and the receding phase and part of the retraction phase of the cavity (for $t^* \geq t^*_{cav,max.}$). A comparison between the curves for the experiments and those for the analytical description and numerical simulations shows that the theoretical description of the diameter of the cavity (eq. (4.10)) and the simulations agree very well with the experimental data for all investigated liquid film thicknesses, Weber numbers and liquids during the expansion and receding phases of the cavity. It is surprising that, although the theory has been developed only for the expansion phase of

the cavity, the agreement during the receding phase of the cavity is for most of the investigated cases very well. Several conditions for such good theoretical predictions of the receding phase can be mentioned. First of all, the thickness of the surface film in the outer region remains approximately equal to the initial surface film thickness, even during the receding phase, as is clearly observed by the Shadowgraph recordings (Figure 4.1). Second, during the receding phase the velocity of the liquid in the outer film is relatively small, resulting in negligibly small values of the inertial terms in the Bernoulli equation (eq. (4.6)) associated with the flow in the outer film. Finally, for impingements at high Reynolds numbers, the influence of the viscosity can be neglected in the experiments. Viscous effects could lead to a decrease of the magnitude of the propagation velocity of the cavity surface. However, in the experiments such a velocity decrease is not observed, since the velocity of the cavity during the receding phase is comparable with the cavity velocity in the spreading phase, hence, viscosity can be neglected.

When comparing the curves of the time evolution of the cavity diameter for different initial liquid film thicknesses, it is observed that an increase in the film thickness leads to a decrease of the steepness of the curves during the expansion phase of the cavity. This means that for single drop impingements onto thicker surface films, but for the same Weber number of the impinging drop, the cavity expands in radial direction with a lower velocity.

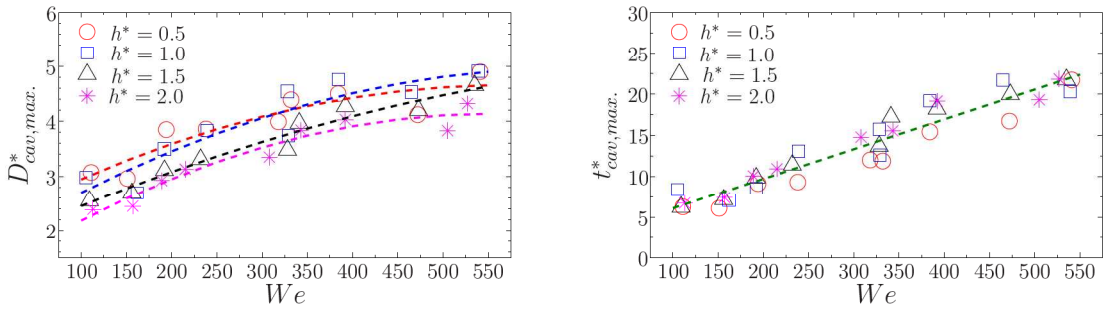

(a) Maximum cavity diameter

(b) Time of maximum cavity diameter

Figure 4.16: Maximum diameter of the cavity and non-dimensional time of the maximum diameter as a function of the initial liquid film thickness and impinging drop Weber number

This lower radial expansion velocity is the result of the increased influence of the surface tension and gravity forces onto the surface of the expanding cavity for larger film thicknesses. Due to these increased surface tension forces and gravity forces on the surface of the cavity the conversion of the kinetic energy of the impinging drop takes place faster, resulting in a lower maximum value of the diameter of the cavity, Figure 4.16(a). Additionally, a lower film thickness leads to earlier times at which the cavity reaches the bottom of the liquid film (Figure 4.21). From this time instant on, all the remaining kinetic energy is used to overcome the surface tension effects during the radial spreading of the cavity. Hence, for the same Weber number of the impinging drop, more kinetic energy is available for the radial expansion of the cavity, when the liquid film is thinner.

Although the maximum diameter of the cavity is influenced by the liquid film thickness, the time instant at which the maximum cavity diameter is reached is independent of the initial liquid film thickness, as presented in Figure 4.16(b). For the receding phase of the cavity little to no difference can be seen when comparing the curves of the time evolution of the cavity diameter for different initial film thicknesses. The decrease of the diameter of the cavity starts slow, but accelerates in time, due to the increased inertial effects. The non-dimensional times

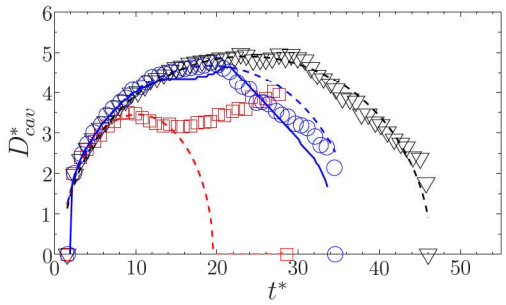

(a) Isopropanol; □: $h^* = 1.0$, $We = 192$, $Re = 1,201$; ◯: $h^* = 1.0$, $We = 384$, $Re = 1,701$; ▽: $h^* = 1.0$, $We = 539$, $Re = 2,013$

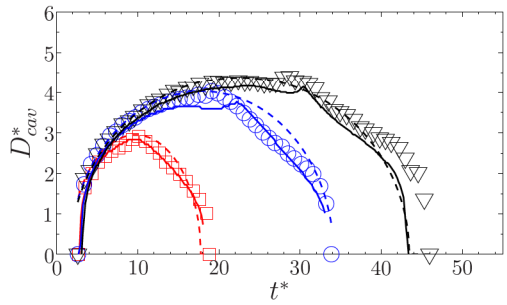

(b) Isopropanol; □: $h^* = 2.0$, $We = 189$, $Re = 1,199$; ◯: $h^* = 2.0$, $We = 392$, $Re = 1,733$; ▽: $h^* = 2.0$, $We = 527$, $Re = 1,982$

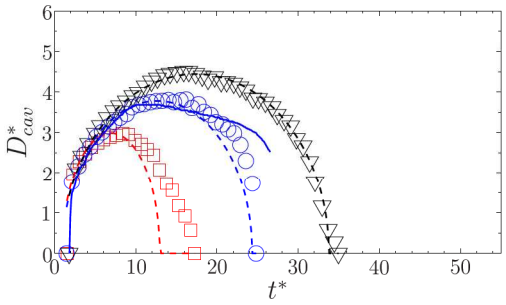

(c) Distilled water; □: $h^* = 1.0$, $We = 105$, $Re = 4,744$; ◯: $h^* = 1.0$, $We = 239$, $Re = 7,241$; ▽: $h^* = 1.0$, $We = 328$, $Re = 8,342$

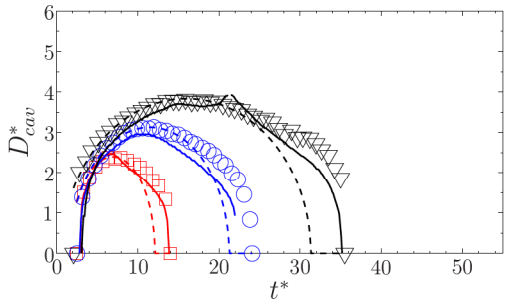

(d) Distilled water; □: $h^* = 2.0$, $We = 113$, $Re = 4,948$; ◯: $h^* = 2.0$, $We = 215$, $Re = 6,750$; ▽: $h^* = 2.0$, $We = 343$, $Re = 8,644$

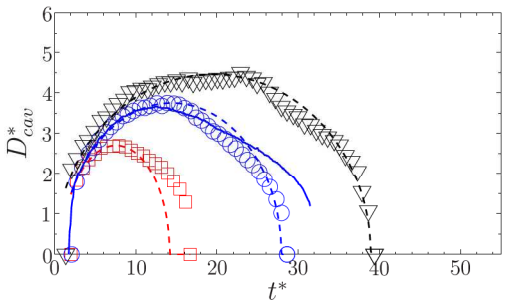

(e) Glycerine/water; □: $h^* = 1.0$, $We = 162$, $Re = 341$; ◯: $h^* = 1.0$, $We = 329$, $Re = 428$; ▽: $h^* = 1.0$, $We = 465$, $Re = 526$

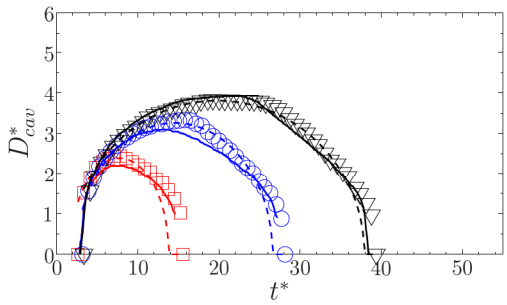

(f) Glycerine/water; □: $h^* = 2.0$, $We = 157$, $Re = 320$; ◯: $h^* = 2.0$, $We = 308$, $Re = 434$; ▽: $h^* = 2.0$, $We = 505$, $Re = 561$

Figure 4.17: Evolution of the diameter of the cavity in time, measured at $y/h^*_{cav} = 0.5$, for the initial film thicknesses of $h^* = 1.0$ (left) and $h^* = 2.0$ (right). Comparison of the experimental results (□, ◯, ▽) with the theoretical predictions (eq. (4.10), dashed line) and the numerical simulations (solid line) for (a)-(b) isopropanol, (c)-(d) distilled water and (e)-(f) glycerine/water. The impingement parameters for the experimental data and the inputs for the analytical model are listed in Table 4.2

at which the diameters of the cavities at $y_{cav}/h^* = 0.5$ equal zero (the cavity passes the vertical point $y_{cav}/h^* = 0.5$ during the retraction phase) are of about the same order of magnitude for different initial film thicknesses. This means that the receding of the cavity takes place in about the same time span for the different film thicknesses, hence, the receding of the cavity is independent of the initial film thickness, but mainly driven by capillary forces.

The influence of the Weber number of the impinging drop on the evolution of the diameter of the cavity in time is shown in Figure 4.17 for $h^* = 1.0$ and $h^* = 2.0$, and in Figure B.7 for $h^* = 0.5$ and $h^* = 1.5$. These figures show the experimentally obtained results for all three liquids, as well as the results of the numerical simulations (solid lines) and of the theoretical approximation (dashed lines).

In the first non-dimensional time instants after impingement a steep growth of the cavity diameter is observed for all Weber numbers, which levels off at the moment the cavity approaches the bottom of the liquid film. The steepness with which the diameter increases, decreases for lower Weber numbers. This is the direct result of the lower kinetic energy of the drop before impingement. During the spreading phase of the cavity the inertial forces are dominant over the capillary forces and gravity effects. For a lower magnitude of the kinetic energy, less energy is available to overcome the surface tension forces acting on the expanding surface of the cavity and opposing the cavity expansion. This results in a less dominant influence of the inertia in comparison with the capillary and gravitational effects. Not only does this result in a lower radial expansion velocity, but also in a smaller value of the time instant at which the maximum cavity diameter is reached (Figure 4.16(b)), leading to a smaller maximum cavity diameter (Figure 4.16(a)). Since the value of the maximum cavity diameter and the time of maximum cavity diameter are smaller for lower Weber numbers and inertia is overcome earlier by capillary forces, the receding of the cavity starts earlier and the non-dimensional time instant at which the cavity passes the vertical point $y_{cav}/h^* = 0.5$ during the retraction phase is reached sooner. This behaviour is seen for all investigated liquids and film thicknesses.

The last investigated parameters that influence the time evolution of the diameter of the cavity are the liquid properties (viscosity and surface tension), of which the results are shown in Figure B.8 for the lowest and medium Weber numbers and in Figure 4.18 for the highest investigated Weber numbers. As has been mentioned already before, the effect of viscosity can be neglected in the impingement process, since the Reynolds numbers for all investigated drop impingements are much higher than unity. The influence of the surface tension on the time evolution of the cavity diameter, however, is much more pronounced. For the three investigated liquids, isopropanol has the lowest surface tension, followed by the glycerine/water mixture and distilled water. For a lower value of the surface tension a much more pronounced spreading of the cavity is observed, resulting from the fact that inertia can overcome easier the surface tension forces opposing the expansion of the cavity, compare for example Figure 4.18(a) (low surface tension) with Figure 4.18(b) (high surface tension). Resulting from the more pronounced spreading of the cavity for liquids with a lower surface tension is a larger value of the maximum cavity diameter, reached at later non-dimensional times after impingement. This is clearly seen in the Figures 4.16(a) and 4.16(b) for, respectively, the value of the maximum cavity diameter and the time of maximum cavity diameter, when taking into account the different values of the Weber numbers for the different investigated liquids.

A lower value of the surface tension leads not only to a wider cavity and therefore larger value of the maximum cavity diameter, but also to weaker surface tension forces acting on the surface of the cavity during the receding phase. This results in a longer receding time and a

later non-dimensional time instant at which the cavity passes the vertical point $y_{cav}/h^* = 0.5$ during the retraction phase, which can be seen clearly by comparing the Shadowgraph images for the three liquids (Figures 4.7 and 4.8).

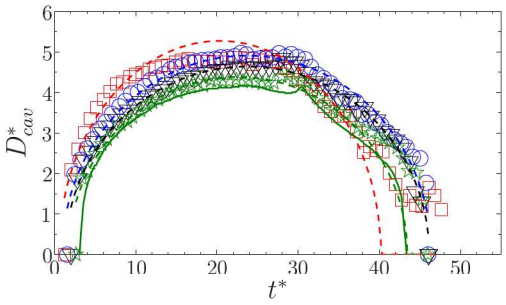

(a) Isopropanol; □: $h^* = 0.5$, $We = 541$, $Re = 2,007$; ◯: $h^* = 1.0$, $We = 539$, $Re = 2,013$; ▽: $h^* = 1.5$, $We = 535$, $Re = 2,006$; ★: $h^* = 2.0$, $We = 527$, $Re = 1,982$

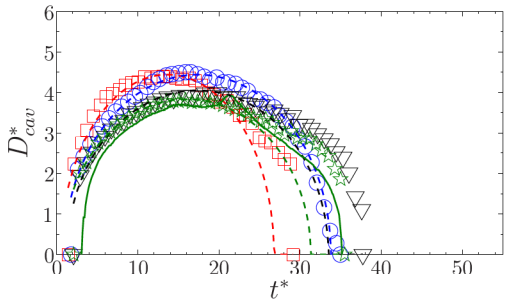

(b) Distilled water; □: $h^* = 0.5$, $We = 332$, $Re = 8,392$; ◯: $h^* = 1.0$, $We = 328$, $Re = 8,342$; ▽: $h^* = 1.5$, $We = 341$, $Re = 8,587$; ★: $h^* = 2.0$, $We = 343$, $Re = 8,644$

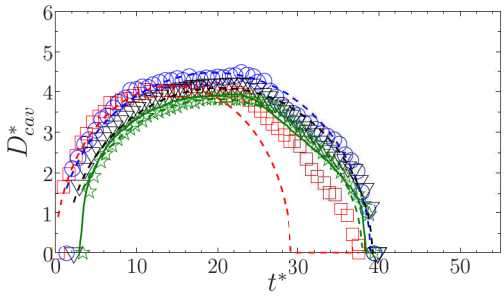

(c) Glycerine/water; □: $h^* = 0.5$, $We = 472$, $Re = 539$; ◯: $h^* = 1.0$, $We = 465$, $Re = 526$; ▽: $h^* = 1.5$, $We = 473$, $Re = 529$; ★: $h^* = 2.0$, $We = 505$, $Re = 561$

Figure 4.18: Evolution of the diameter of the cavity in time, measured at $y/h^*_{cav} = 0.5$, for the largest drop Weber numbers and four film thicknesses. Comparison of the experimental results (□, ◯, ▽, ★) with the theoretical predictions (eq. (4.10), dashed line) and the numerical simulations (solid line) for (a) isopropanol, (b) distilled water and (c) glycerine/water. The impingement parameters for the experimental data and the inputs for the analytical model are listed in Table 4.2

4.3 Evolution of the depth of the cavity in time

This paragraph presents the detailed results of the depth evolution of the cavity in time upon impingement of a single drop onto a steady liquid film of finite thickness. In the experiments the depth is measured at the lowest point of the cavity observed in the Shadowgraph recordings, whereas for the analysis of the numerical simulations, the depth is determined using the computational cells where the volume fraction becomes $\gamma \geq 0.5$. The results of the experiments are compared with the analytical models derived in Beberovic *et al.* [10] and the numerical

simulations to validate the theoretical models and the numerical code. Several particular impingements of the many impingement experiments conducted are selected and presented in more detail hereafter. The impingement parameters of all the experiments, together with the inputs for the analytical models, are listed in Table 4.2.

In the following paragraphs the impingement process is split up into two parts: the initial phase of drop impingement and the complete impingement process. The initial impingement stage spans a non-dimensional time range between $t^* = 0$ and $t^* \approx 5$ and is used to evaluate the models, that describe the initial depth penetration. In the paragraph thereafter the complete drop impingement process will be evaluated, in which the experimental data of the depth evolution of the cavity in time will be compared with the analytical models and the numerical simulations.

4.3.1 Initial phase of drop impingement

In Beberovic *et al.* [10] a theoretical model has been derived for the description of the penetration depth of the cavity at the initial stage of drop impingement. It was found that the analytical solution of the depth of the cavity can be written as a function of the non-dimensional time by:

$$y^*_{cav} = 0.574 \cdot (5t^* - 6)^{2/5}, \qquad t^* > 2 \tag{4.18}$$

Since the cavity penetrates into the liquid film with a constant vertical velocity, independent of the drop impingement Weber number, liquid properties and initial film thickness, it can be expected that this general equation for the penetration depth at initial stage of drop impingement can be used to describe the cavity penetration. In order to validate this analytical solution, the experimental data for the cavity penetration lengths for various impingement parameters and non-dimensional initial film thicknesses are shown in Figure 4.19 together with the analytical asymptotic solution described by eq. (4.18) for the penetration depth at initial stage of drop impingement.

In this figure it can be seen that right after impingement all curves for the depth of the cavity follow quite well the analytical solution, but that a the non-dimensional time instant $t^* = 2.5$ the experimental data start to deviate from the analytical solution. This deviation is determined by the initial film thickness, or more precisely, by the vicinity of the cavity tip to the bottom of the liquid film. A smaller initial film thickness leads to an earlier deviation from the asymptotic solution which is developed for deep pools, compare for example $We = 328, Re = 8,342$ for $h^* = 1$ with $We = 215, Re = 6,750$ for $h^* = 2$. These results also demonstrate that wall effects may be significant already at the initial stages of drop impingement.

4.3.2 Later stages of drop impingement

In this section the influences of the initial liquid film thickness, the Weber number of the impinging drop, and the liquid properties (surface tension and viscosity) on the complete evolution of the cavity depth are investigated and explained. From all the experimental data a selected group is shown in this section; the results of all the remaining conducted experiments can be found in Appendix B.

Plots of the non-dimensional cavity depth ($Depth^*_{cav}$) against the non-dimensional time (t^*) for the four investigated initial liquid film thicknesses are given in Figure 4.20 for distilled water, in Figure B.1 for isopropanol and in Figure B.2 for the glycerine/water mixture. The symbols

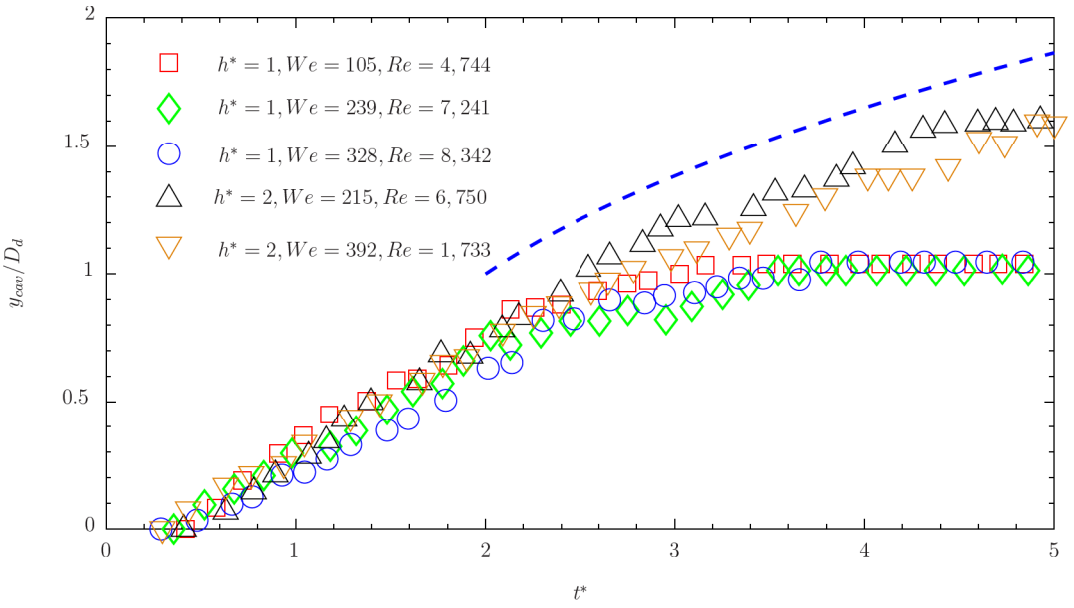

Figure 4.19: Drop impingement onto a liquid film of finite thickness: experimentally obtained penetration depth of the cavity (symbols) as a function of time for various film thicknesses compared to the asymptotic solution (eq. (4.18), Beberovic *et al.* [10]) for the first time instants after drop impingement

in the figures correspond to the experimental data, whereas the solid lines are the results of the numerical simulations.

The first important observation is that the numerical simulations predict very well the time evolutions of the cavities after impingement for all the investigated film thicknesses, impinging drop Weber numbers and liquids. This means that the modified volume-of-fluid code, presented in Beberovic *et al.* [10], is suited very well for the prediction of the single drop impingement process.

Right after impingement a steep increase in the depth of the cavity is noticed for all the curves. In all three figures it can be seen that the penetration velocity of the cavity into the liquid film is constant and thus independent of the initial liquid film thickness, as has been mentioned already in the discussion of the impingement observations, presented in §(4.1). This non-dimensional penetration velocity of the cavity equals $U^*_{cav} = 0.5$. At the time instant at which the cavity nearly touches the bottom of the liquid film, the influence of the bottom becomes stronger, resulting in a decrease of the velocity with which the cavity penetrates into the liquid layer and subsequent leveling of the curves of the depth of the cavity. This influence of the bottom of the liquid film on the depth penetration of the cavity, together with the influence of gravity and capillary effects, explains the deviation of the experimentally obtained cavity depth from the analytical model, shown in Figure 4.19. The times at which the cavities reach the bottom of the liquid films are shown in Figure 4.21 as a function of the initial liquid film thickness and Weber number for all three investigated liquids.

As expected for a penetration velocity of the cavity that is constant and independent of the initial liquid film thickness, an increase in the film thickness leads automatically to an increase in the time instant at which the cavity reaches the bottom of the liquid film. This increase is

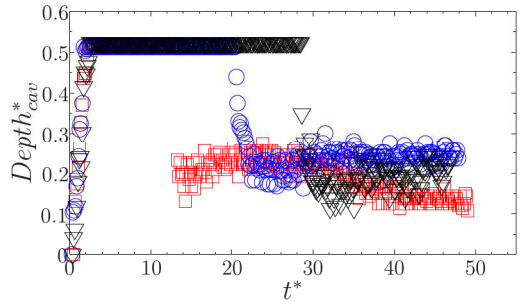

(a) Distilled water; □: $h^* = 0.5$, $We = 111$, $Re = 4,871$; ◯: $h^* = 0.5$, $We = 238$, $Re = 7,173$; ▽: $h^* = 0.5$, $We = 332$, $Re = 8,392$

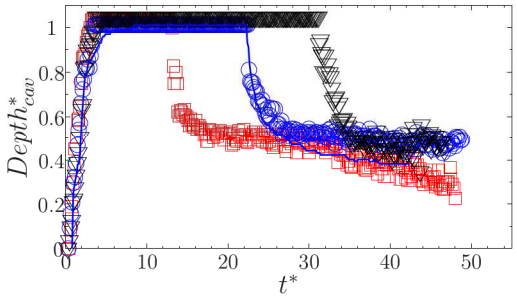

(b) Distilled water; □: $h^* = 1.0$, $We = 105$, $Re = 4,744$; ◯: $h^* = 1.0$, $We = 239$, $Re = 7,241$; ▽: $h^* = 1.0$, $We = 328$, $Re = 8,342$

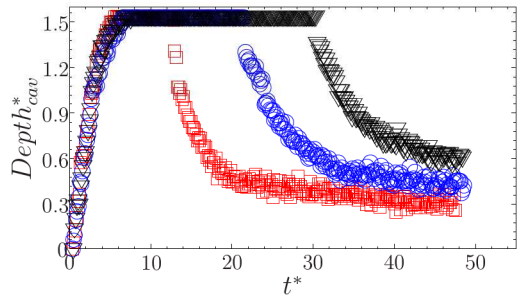

(c) Distilled water; □: $h^* = 1.5$, $We = 110$, $Re = 4,870$; ◯: $h^* = 1.5$, $We = 232$, $Re = 7,115$; ▽: $h^* = 1.5$, $We = 341$, $Re = 8,587$

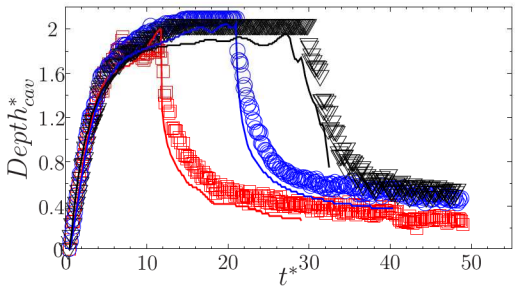

(d) Distilled water; □: $h^* = 2.0$, $We = 113$, $Re = 4,948$; ◯: $h^* = 2.0$, $We = 215$, $Re = 6,750$; ▽: $h^* = 2.0$, $We = 343$, $Re = 8,644$

Figure 4.20: Evolution of the depth of the cavity in time for different initial film thicknesses. Comparison of the experimental results (□, ◯, ▽) with the numerical simulations (solid line) for distilled water. The impingement parameters for the experimental data and the inputs for the analytical model are listed in Table 4.2

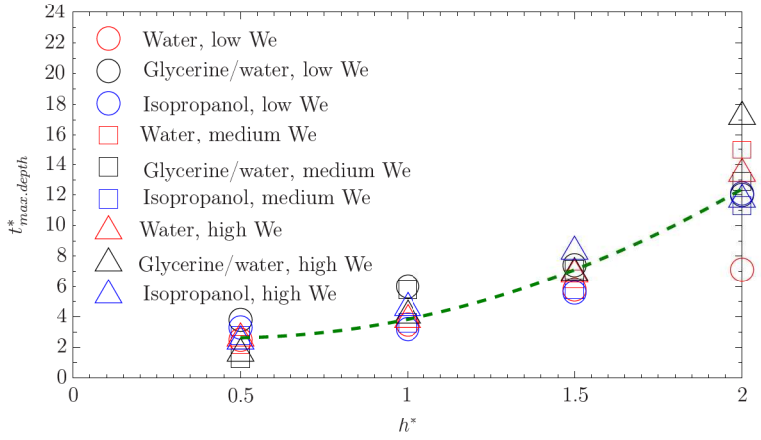

Figure 4.21: Time to reach maximum depth of cavity as a function of the initial liquid film thickness and impinging drop Weber number

however not linear, as would be expected for a constant penetration velocity, since for higher film thicknesses the time span in which the curve of the depth of the cavity levels off increases, compare for example Figure B.3(c) with Figure 4.23(d) for $h^* = 0.5$ and $h^* = 2.0$ respectively. In the first figure the time for leveling of the curves is negligibly small, whereas for a film thickness of $h^* = 2$ it takes about eight non-dimensional time steps between the first changes in penetration velocity and the time at which the cavities have reached the bottom of the liquid film. This difference is explained by the difference in value of the kinetic energy that is still available at a certain depth. In case of the same Weber number of the impinging drop, the bottom of the liquid film is reached sooner for lower film thicknesses. This shorter time span between impingement and the moment the cavity nears the bottom results in a cavity with a smaller diameter, as was shown before in the discussion of the diameter evolution of the cavity, and therefore inertia has to overcome less surface tension forces. For larger film thicknesses the cavity can penetrate vertically into the liquid film for a longer time, during which it also continues expanding in radial direction. This results in larger surface tension forces opposing the expansion of the cavity, that have to be overcome by inertia for a longer time. At later time instants after impingement less kinetic energy is available to overcome the surface tension forces, leading to a penetration velocity that becomes weaker at every subsequent time instant.

After the cavities have reached the bottom of the liquid films, they reside a certain period near the bottom, which is seen in the figures as horizontal lines of constant cavity depth. When looking closer to the results of the numerical simulations, it can be seen that, in comparison to the experimental results, the cavities stay close to the bottom of the liquid films, but do not touch them (see, for example, the numerical calculated shapes of the cavity for distilled water and isopropanol, Figure 4.9 and 4.10) Due to the limited spatial resolution of the camera with which the shadowgraph images were made (18.9 $\mu m/pix$) and the presence of the cavity reflections on the bottom of the plexiglass container, it is not possible to define the exact maximum depths of the cavities close to the bottom of the liquid films in an experimental way. Since for the numerical simulations grid refinements are applied at the bottom of the liquid film, this leads to the small differences in the values of the depth of the cavities for the experimental results and the numerical simulations. The values of the numerically obtained residual film thicknesses, still present below the cavity at maximum depth, will be discussed in §(4.5).

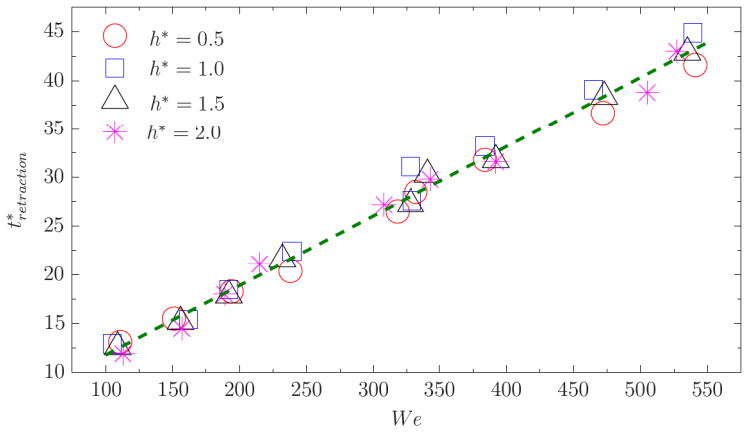

Figure 4.22: Time of retraction of the cavity as a function of the initial liquid film thickness and impinging drop Weber number

It is observed that for lower Weber numbers the cavities stay at their maximum depths for a longer time period, before retraction of the cavities takes place. The time between impingement and the retraction of the cavity is shown in Figure 4.22 as a function of the initial liquid film thickness and Weber number for all three investigated liquids. This figure shows that for a fixed Weber number of the impinging drop a change in the liquid film thickness does not change the time at which the cavity starts to retract. A larger Weber number, however, leads to a later retraction of the cavity, as can also be observed when comparing the curves of the depth evolutions of the cavities in the Figures 4.20, B.1 and B.2. The explanation for this increase of the time instant of cavity retraction will be given in the next section.

At the beginning of the retraction phase, the retraction velocities of the cavities are large, due to the strong influence of the surface tension forces on the surface of the cavity. As time continues, the curves start to level off, because the surface of the upward moving cavities becomes smaller, leading to weaker surface tension forces acting on the cavity.

The second parameter that is changed during the single drop impingement studies, is the Weber number of the impinging drop. The influence of the Weber number of the impinging drop on the evolution of the depth of the cavity in time is shown in Figure 4.23 for $h^* = 1.0$ and $h^* = 2.0$, and in Figure B.3 for $h^* = 0.5$ and $h^* = 1.5$. These figures show the experimentally obtained results for all three liquids, as well as the results of the numerical simulations.

The first remarkable observation made by looking at the depth evolution of the cavity for different Weber numbers of the impinging drop is that the velocity with which the cavity penetrates into the liquid film after impingement is independent of the terminal velocity of the drop before impingement, and equals $U^*_{cav} = 0.5$ for all drop Weber numbers.

During the penetration and receding phase of the cavity it is noted that the Weber number of the impinging drop has little to no effect on the time evolution of the depth of the cavity for all investigated liquids and liquid film thicknesses. This independency on the Weber number can also be seen for the investigation of the time at which the cavity reaches the bottom of the liquid film, Figure 4.21. In this figure it is observed that for each of the liquid films investigated a change in Weber number has no influence on the time at which the cavity reaches its maximum depth, although for $h^* = 2.0$ some scatter in the data can be seen.

The only clear effect of a change of the Weber number on the time evolution of the cavity depth is the time instant at which the cavity starts to retract. An increase in the Weber number results in a later retraction of the cavity, as was observed already in the Figures 4.5 and 4.6 where the Shadowgraph images were shown for the impingement of a distilled water drop for three different Weber numbers. This behaviour is observed for all investigated liquids and liquid film thicknesses (Figure 4.22), and is the result of the higher kinetic energy of the impinging drop present upon impingement for higher Weber numbers. Due to more kinetic energy, the surface tension forces, acting on the increasing surface of the growing cavity, can be overcome by inertia for a longer time, resulting in a later receding of the cavity, hence, longer times at which the cavity stays at its maximum depth, thus a later retraction of the cavity.

By changing the liquids, the influence of the liquid properties (viscosity and surface tension) on the time evolution of the depth of the cavity can be investigated. The properties of each of the liquids has been given in Table 3.1. The results for the evolution of the depth of the cavity in time are shown in Figure B.4 for the lowest and medium Weber numbers investigated, and in Figure 4.24 for the highest investigated Weber numbers. In each of these figures the experimentally obtained results for all four investigated liquid film thicknesses, as well as the results of the numerical simulations, are presented.

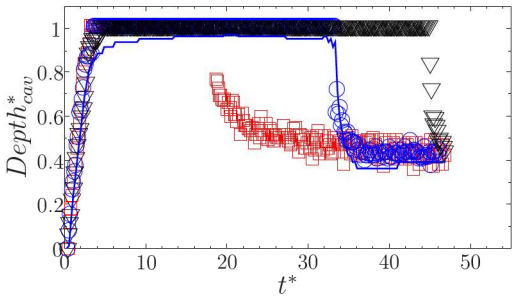

(a) Isopropanol; □: $h^* = 1.0$, $We = 192$, $Re = 1,201$; ◯: $h^* = 1.0$, $We = 384$, $Re = 1,701$; ▽: $h^* = 1.0$, $We = 539$, $Re = 2,013$

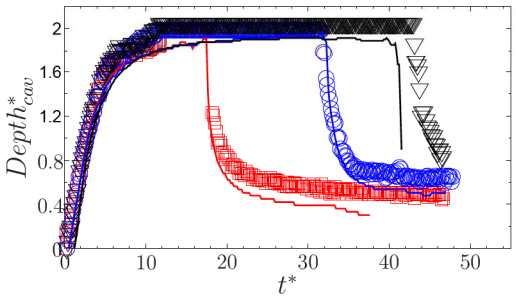

(b) Isopropanol; □: $h^* = 2.0$, $We = 189$, $Re = 1,199$; ◯: $h^* = 2.0$, $We = 392$, $Re = 1,733$; ▽: $h^* = 2.0$, $We = 527$, $Re = 1,982$

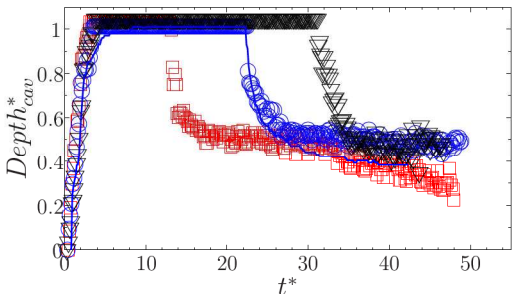

(c) Distilled water; □: $h^* = 1.0$, $We = 105$, $Re = 4,744$; ◯: $h^* = 1.0$, $We = 239$, $Re = 7,241$; ▽: $h^* = 1.0$, $We = 328$, $Re = 8,342$

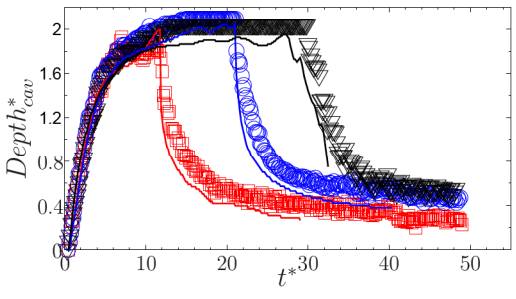

(d) Distilled water; □: $h^* = 2.0$, $We = 113$, $Re = 4,948$; ◯: $h^* = 2.0$, $We = 215$, $Re = 6,750$; ▽: $h^* = 2.0$, $We = 343$, $Re = 8,644$

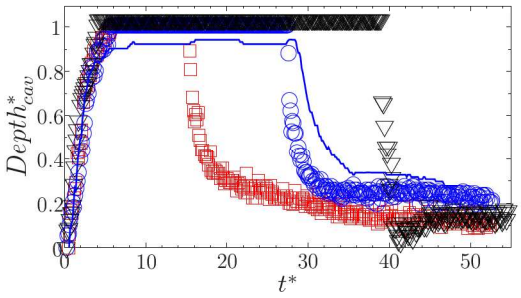

(e) Glycerine/water; □: $h^* = 1.0$, $We = 162$, $Re = 341$; ◯: $h^* = 1.0$, $We = 329$, $Re = 428$; ▽: $h^* = 1.0$, $We = 465$, $Re = 526$

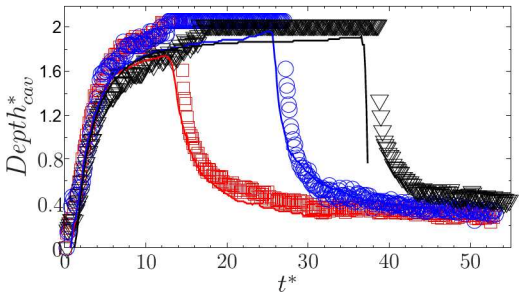

(f) Glycerine/water; □: $h^* = 2.0$, $We = 157$, $Re = 320$; ◯: $h^* = 2.0$, $We = 308$, $Re = 434$; ▽: $h^* = 2.0$, $We = 505$, $Re = 561$

Figure 4.23: Evolution of the depth of the cavity in time for the initial film thicknesses of $h^* = 1.0$ (left) and $h^* = 2.0$ (right). Comparison of the experimental results (□, ◯, ▽) with the numerical simulations (solid line) for (a)-(b) isopropanol, (c)-(d) distilled water and (e)-(f) glycerine/water. The impingement parameters for the experimental data and the inputs for the analytical model are listed in Table 4.2

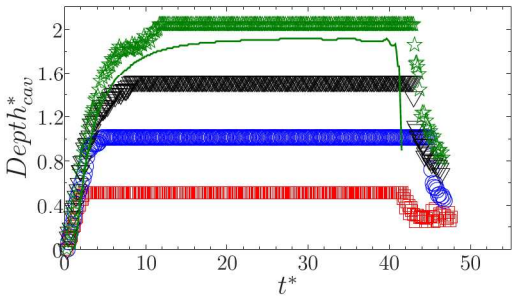

(a) Isopropanol; □: $h^* = 0.5$, $We = 541$, $Re = 2,007$; ◯: $h^* = 1.0$, $We = 539$, $Re = 2,013$; ▽: $h^* = 1.5$, $We = 535$, $Re = 2,006$; ★: $h^* = 2.0$, $We = 527$, $Re = 1,982$

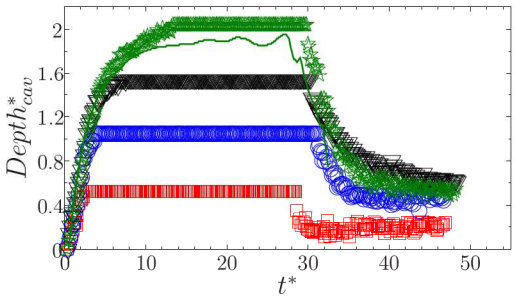

(b) Distilled water; □: $h^* = 0.5$, $We = 332$, $Re = 8,392$; ◯: $h^* = 1.0$, $We = 328$, $Re = 8,342$; ▽: $h^* = 1.5$, $We = 341$, $Re = 8,587$; ★: $h^* = 2.0$, $We = 343$, $Re = 8,644$

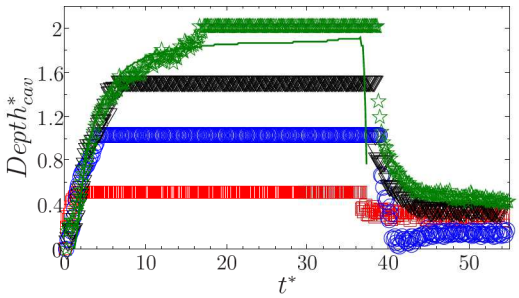

(c) Glycerine/water; □: $h^* = 0.5$, $We = 472$, $Re = 539$; ◯: $h^* = 1.0$, $We = 465$, $Re = 526$; ▽: $h^* = 1.5$, $We = 473$, $Re = 529$; ★: $h^* = 2.0$, $We = 505$, $Re = 561$

Figure 4.24: Evolution of the depth of the cavity in time for the largest drop Weber numbers and four film thicknesses. Comparison of the experimental results (□, ◯, ▽, ★) with the numerical simulations (solid line) for (a) isopropanol, (b) distilled water and (c) glycerine/water. The impingement parameters for the experimental data and the inputs for the analytical model are listed in Table 4.2

In general it can be said that due to the high Reynolds numbers for all the investigated impingement processes the influence of viscosity on the time evolution of the depth of the cavity is expected to be negligible. This is confirmed when looking at the curves for the different liquids. These curves clearly show that a change in the liquids properties has no influence on the velocity with which the cavity penetrates into the liquid film after impingement. The penetration velocity remains constant for all three investigated liquids and equals $U^*_{cav} = 0.5$. This clearly shows that for large Weber numbers, Reynolds numbers and Froude numbers the effects of, respectively, surface tension, viscosity and gravity on the cavity penetration can be neglected, hence, the cavity penetrates into the liquid film only due to inertia. Just like for the change in Weber number of the impinging drop, a change in viscosity and/or surface tension has little to no effect on the time evolution of the cavity depth during the penetration and receding phases. The time at which the cavity reaches the bottom of the liquid film is independent of the liquid properties, as can be seen in Figure 4.21.

However, a change of the liquid properties has a clear effect on the time instant at which the cavity starts to retract. A decrease in the surface tension results in a later retraction of the cavity, as was observed in the Figures 4.7 and 4.8 where a comparison of the Shadowgraph recordings was made for the three investigated liquids. This behaviour is observed for all investigated Weber numbers and liquid film thicknesses (Figure 4.22). For a constant value of the Weber number of the impinging drop, the surface tension forces, acting on the increasing surface of the growing cavity, are weaker for isopropanol, due to the lower value of the surface tension, and can be overcome by inertia for a longer time, resulting in a later receding of the cavity and thus a later retraction of the cavity.

4.4 Fully three-dimensional simulation of drop impingement

Since the axi-symmetric simulations, presented above, are not capable of describing precisely the three-dimensional nature of the flow of the corona, hence the rim instability and secondary droplet pinch-off, a full three-dimensional computational model is used, taking into account the physical perturbations leading to instability. A comparison between the evolution of the shape of the cavity for the axi-symmetric numerical simulations and the fully three-dimensional simulations is presented hereafter. Although the experiments are fully three-dimensional and therefore small errors are to be expected between the experimental results and the numerical simulations, it was seen in the discussion of the results above that the correlation between the time evolution of the cavity depth and cavity diameter for the experiments and for the numerical simulations is surprisingly good. In this paragraph it will be shown that the influence of the three-dimensional effects on the shape of the cavity are only minor, hence, the axi-symmetric numerical results can be used for the detailed analysis of the change of the cavity in time.

To investigate the possible errors of the axi-symmetrical simulations on the cavity evolution, a fully three-dimensional computational model is used, taking into account the physical perturbations leading to instability. In this paragraph a comparison between the evolution of the shape of the cavity for the axi-symmetric numerical simulations and the fully three-dimensional simulations will be made. It will be shown that the influence of the three-dimensional effects on the shape of the cavity, which appear during the receding phase, are only minor, hence, the axi-symmetric numerical results give a good analysis of the change of the cavity in time and much computational time can be saved.

In figure 4.25 the time evolution of the cavity shape for the axi-symmetrical simulation (thick lines) and the fully three-dimensional numerical simulation (thin lines) are presented.

The images show that until a non-dimensional time instant of $t^* = 22.9$ no differences of the cavity can be observed between the two different simulations. Concerning the rim, however, a clear difference in shape is seen. The results of the axi-symmetrical simulation show a relatively thick rim, whereas for the three-dimensional simulation the rim starts very thin (Figure 4.25(b) and 4.25(c)) and becomes thicker for larger times after impingement. The curvature of the free surface is also seen to be smaller for the three-dimensional case. These differences in the shape of the rim can be explained by two parameters. First of all, the axi-symmetrical simulation cannot resolve the three-dimensional flow of the rim, meaning that the rim will always be simulated as a torus, having exactly the same circumferential shape at every azimuthal position. This problem is avoided by a fully three-dimensional simulation, in which case the three dimensional flow can be resolved in detail. Second, the grid for the fully three-dimensional simulation is

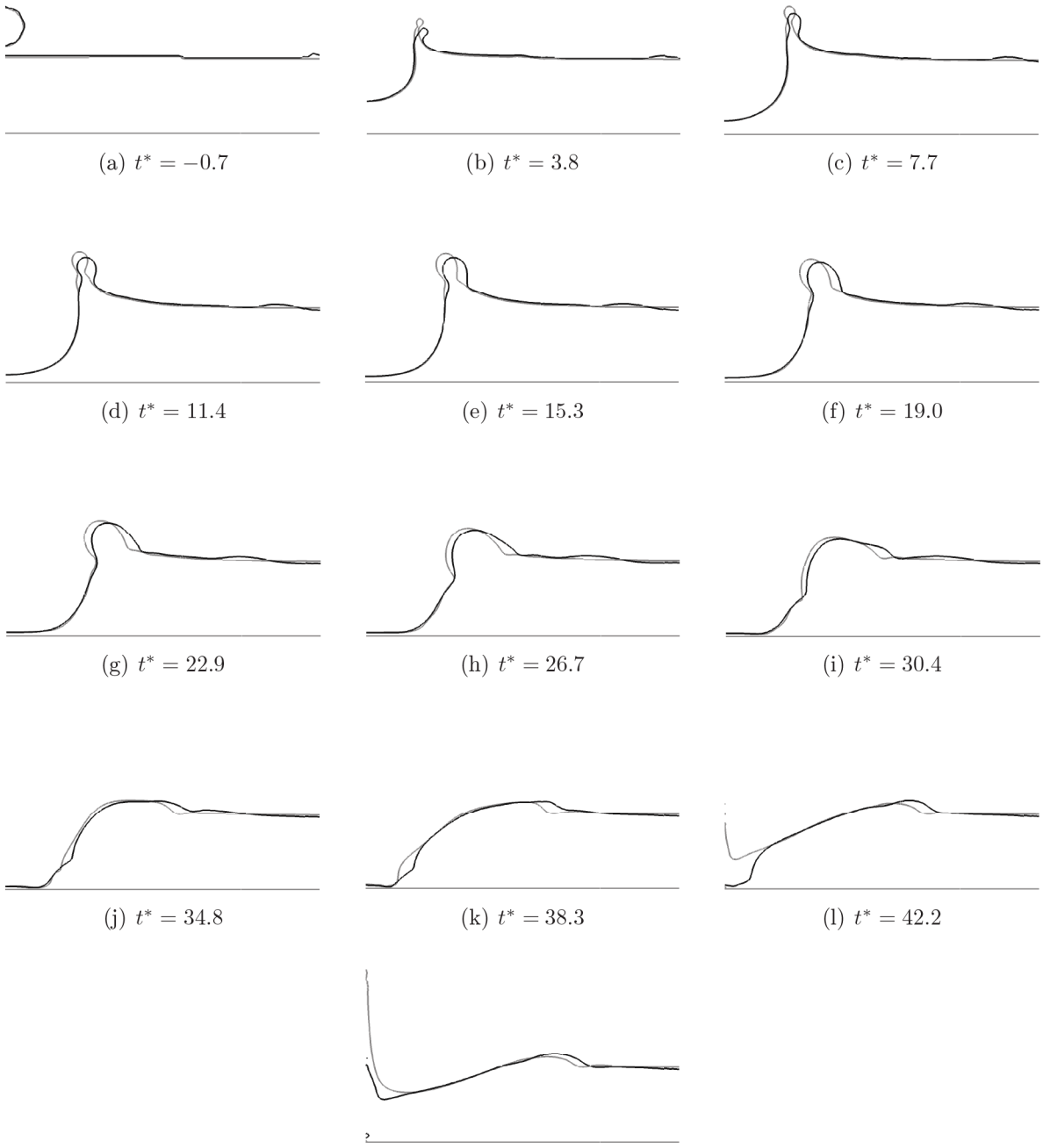

(a) $t^* = -0.7$ (b) $t^* = 3.8$ (c) $t^* = 7.7$

(d) $t^* = 11.4$ (e) $t^* = 15.3$ (f) $t^* = 19.0$

(g) $t^* = 22.9$ (h) $t^* = 26.7$ (i) $t^* = 30.4$

(j) $t^* = 34.8$ (k) $t^* = 38.3$ (l) $t^* = 42.2$

(m) $t^* = 46.1$

Figure 4.25: Comparison of the cavity shape between the axi-symmetrical (thin solid lines) and the fully three-dimensional (thick solid lines) numerical simulation of a single drop impingement onto a liquid layer of non-dimensional thickness $h^* = 2$, Fromm [44]. The evolution of the cavity formed by an isopropanol drop ($We = 527$, $Fr = 366$, $Re = 1,982$) impingement at various non-dimensional time instants

quite coarse to avoid large computational times, but this has a clear effect on the resolution with which the thin rim can be calculated and imaged.

For non-dimensional times $t^* \geq 26.7$ it can be observed that the capillary wave has a higher vertical velocity in case of the axi-symmetrical simulation. This is the result of a stronger curvature of the capillary wave for the axi-symmetrical case, leading to a higher pressure difference between the trailing and the leading edge of the capillary wave. This higher pressure difference results in a higher velocity and higher acceleration with which the capillary wave is sucked downwards into the liquid film. Due to the higher vertical velocity of the capillary wave, the receding phase of the cavity takes place faster, since the capillary wave reaches the bottom of the liquid film at a non-dimensional time instant of $t^* = 38.3$ for the axi-symmetrical simulation and at $t^* = 42.2$ for the three-dimensional simulation. At $t^* = 42.2$ a thin liquid film is still present for the three-dimensional case, whereas for the axi-symmetrical simulation the cavity is retracting and the central jet is being formed. It can be seen in Figure 4.25(m) that for the three-dimensional simulation a small air bubble has pinched off from the cavity during the receding phase, whereas for the axi-symmetrical case no such bubble pinch-off appears.

The comparison of the time evolution of the depth and the diameter of the cavity between the experimental results, the theoretical prediction and the axi-symmetrical and three-dimensional simulations is shown in Figure 4.26. In this figure, the symbols correspond to the experimental data, the dashed-dotted line to the theoretical predictions and the solid line and dashed line to, respectively, the axi-symmetrical and three-dimensional simulations.

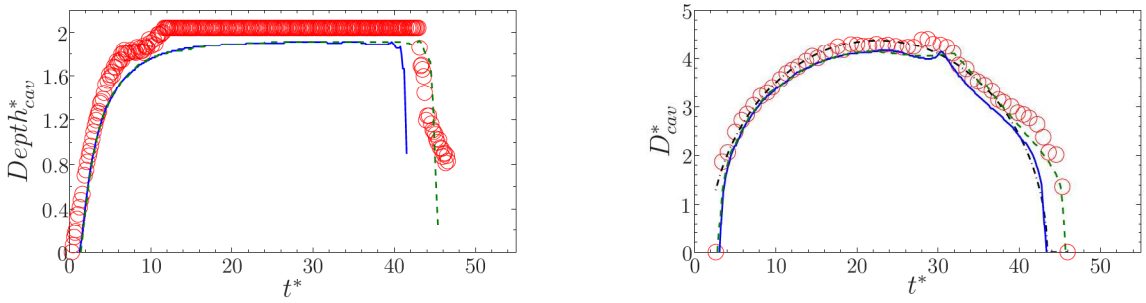

(a) Time evolution of cavity depth

(b) Time evolution of cavity diameter

Figure 4.26: Evolution of the depth (a) and the diameter (b) of the cavity in time. Comparison of the experimental results (◯) with the theoretical approximation (−·) and the numerical simulations (solid line: axi-symmetrical; dashed line: three-dimensional) for isopropanol ($h^* = 2.0$, $We = 527$, $Re = 1,982$)

By comparing the results for the time evolution of the depth and the diameter of the cavity of both simulations it is seen that for the three-dimensional simulation the correlation with the experimental data is much better. For non-dimensional time instants $t^* \leq 30$ only minor differences are seen to occur between the results of the two numerical simulations for the time evolution of the cavity depth. The oscillations in the cavity depth, present at $t^* \geq 30$ for the axi-symmetrical simulation, disappear for the three-dimensional case, but these differences have no influence on the minimum residual film thickness, as will be shown in §(4.5).

Since the curvature of the capillary waves and the subsequent pressure difference and vertical velocity of the capillary wave are higher in the axi-symmetrical simulation, the receding phase of the cavity starts in this case sooner and spans a shorter time (Figure 4.25), leading

to large differences for the cavity diameter between the axi-symmetrical simulation and the experimental data. For the three-dimensional simulation Figure 4.26(b) shows a much better correlation with the experiments; the time at which the cavity starts to recede is captured very well, as well as the times at which the cavity starts its retraction and at which the central jet is being formed (Figure 4.26(a)).

In general, these results show that for the expansion phase of the cavity the axi-symmetrical results are reliable and can be used without any doubt. Since, however, the fully three-dimensional simulation can resolve in detail the three-dimensional flow of the rim, this results in a different shape of the rim for both simulations. The capillary wave, formed upon impingement of the rim onto the liquid film, will therefore be formed in a different way, leading to a receding of the cavity which is slower for the fully three-dimensional simulation. In this way the time at which the cavity starts to recede, the diameter evolution of the receding cavity and the time of cavity retraction are captured better by the fully three-dimensional numerical simulation.

However, the small errors, appearing in the receding phase for the axi-symmetrical simulation, can be taken into account when looking at the computational time, which is about an order of magnitude six smaller.

4.5 Minimum residual film depth

Spray cooling is a very efficient way of (rapidly) cooling down a surface or keeping a cold surface at a constant temperature. The spray constantly refreshes the liquid surface film, which is heated up by the hot surface, with new cold liquid and removes efficiently the heat from the hot surface. In order to understand the physics behind the spray cooling process, it is important to know the specific characterisations of the spray (drop velocity and diameter distributions, volume fluxes) and the surface film fluctuations and to understand the velocity fields inside the surface film, which give an indication in which direction and how fast the heat is being transported away from the hot surface, which parts of the hot surface are being cooled less and how fast the warm liquid is being refreshed by new cold liquid.

However, at the same time it is necessary to understand perfectly the single drop impingement process, in order to theoretically describe the heat flow from the hot surface to the cold liquid surface film during impingement. One of the key parameters in describing the heat fluxes is the value of the residual liquid film h^*_{res} that is still present below the cavity at its maximum depth. This residual film thickness is a measure of how much cold liquid is still present on the hot surface during impingement, whether film break-up appears - as a result of which no more heat conduction can take place between the hot surface and the liquid film - and how much heat can be transported away from the hot surface inside a certain time period.

4.5.1 Theoretical analysis of the minimum residual film thickness

When the cavity approaches the bottom of the liquid film, the penetration velocity decreases due to the wall effects. When the inertia of the liquid flow is strong enough, the thickness of the film below the cavity follows the remote asymptotic solution given by Yarin and Weiss [196] and decreases with t^{-2}. At some time instant after impingement the thickness of the liquid film still present below the cavity becomes comparable with the thickness of the viscous boundary layer. The flow in this thin liquid layer is damped by viscosity. The remaining thin liquid film thickness h is much smaller than the initial thickness of the liquid layer h^*, see Figure 4.11.

This phase corresponds to the "plateau"-region, where the depth of the cavity is no function of time anymore.

The value of the residual film thickness is rather important for the modeling of heat transfer associated with drop or spray impingement and prediction of the film breakup. Unfortunately, since the residual film thickness is much smaller than the initial drop diameter and the initial surface film thickness, its experimental evaluation is not an easy task. For the impingement processes presented hereafter, this value is determined from the numerical simulations. The predicted values of the residual film thickness $h^*_{res} = h_{res}/D_d$ are given in the paragraph hereafter for various impingement parameters and liquids.

The thickness of the boundary layer at the dimensionless time t^*_b at which the cavity almost reaches the bottom can be approximated by:

$$h^*_b \sim \sqrt{t^*_b/Re} \tag{4.19}$$

When the cavity approaches the bottom, the film thickness below the cavity follows the remote asymptotic solution (Yarin and Weiss [196]). At larger times after impingement, this film thickness and the velocity with which the surface of the cavity expands can be written in the simplified forms:

$$h^*_{cav} = h^* - y^*_{cav} \sim t^{*-2} \tag{4.20}$$

$$U^*_{cav} = \frac{dh^*_{cav}}{dt} \sim t^{*-3} \tag{4.21}$$

Therefore, the time instant at which the boundary layer reaches the free surface of the cavity is $t^*_b \sim Re^{1/5}$ and the cavity velocity at this time instant is $U^*_{cav} \sim Re^{-3/5}$. The film thickness h^*_b corresponding to the time instant t^*_b can be easily estimated from eq. (4.20) as $h^*_b \sim Re^{-2/5}$.

The residual film thickness is smaller than h^*_b, since the inertia of the fluid at the time instant $t^* = t^*_b$ is still significant. The value of the residual film thickness is estimated assuming the creeping flow in the film (Bakshi *et al.* [7]) in the following form:

$$h^*_{res} = h_b^{9/14} \cdot \left(\frac{1}{h^*_b} + \frac{14ReU^*_{cav}}{15} \right)^{-5/14} \tag{4.22}$$

With the scaling analysis for h^*_{cav} and U^*_b as function of the Reynolds number, this equation leads to the following relation between the residual film thickness and the Reynolds number:

$$h^*_{res} = ARe^{-2/5} \tag{4.23}$$

The coefficient A depends on the non-dimensional initial film thickness h^*, as well as on the Weber number and Froude number. However, the dependency on We and Fr is weak if these numbers are much larger than unity.

For most of the conducted numerical simulations, oscillations in the film thickness below the cavity after impingement can be observed at time instants at which the minimum residual film thickness is neared. These oscillations are the result of the combination of two phenomena occurring simultaneously: the downward motion of the capillary waves and the contraction of the cavity in radial direction. In most of the simulations these oscillations appear after the residual film thickness has reached its minimum value, due to which a "plateau" in the evolution of the residual film thickness is observed, out of which the absolute minimum residual

film thickness can be determined easily. For some simulations, however, the oscillations in the film thickness appear already before the minimum residual film thickness is reached, making it difficult to assign an absolute minimum for the residual film thickness.

In order to obtain the residual film thickness from the simulations in case of residual film oscillations, an algebraic model, based on a curve fitting tool, is used, which is described by the following expression:

$$h^*_{res,approx} = \frac{c_1}{(t^* + c_2)^2} + c_3 \tag{4.24}$$

Here c_1, c_2 and c_3 are constants, which depend on the Reynolds number and on the initial film thickness h^*. Since the approximation and the film thickness obtained by the numerical simulations converge asymptotically towards the residual film thickness, the absolute minimum residual film thickness can be obtained by eq. (4.24) as $h^*_{res,approx} = c_3$.

The optimum time range relevant for the approximation of the absolute minimum residual film thickness is shown in Figure 4.27. The time range for the approximation starts at about $t^* = 2$, since this model cannot reproduce the drop impingement phase correctly, and finishes at the time instant at which the capillary waves arrive at the center of the cavity leading to the closure of the cavity.

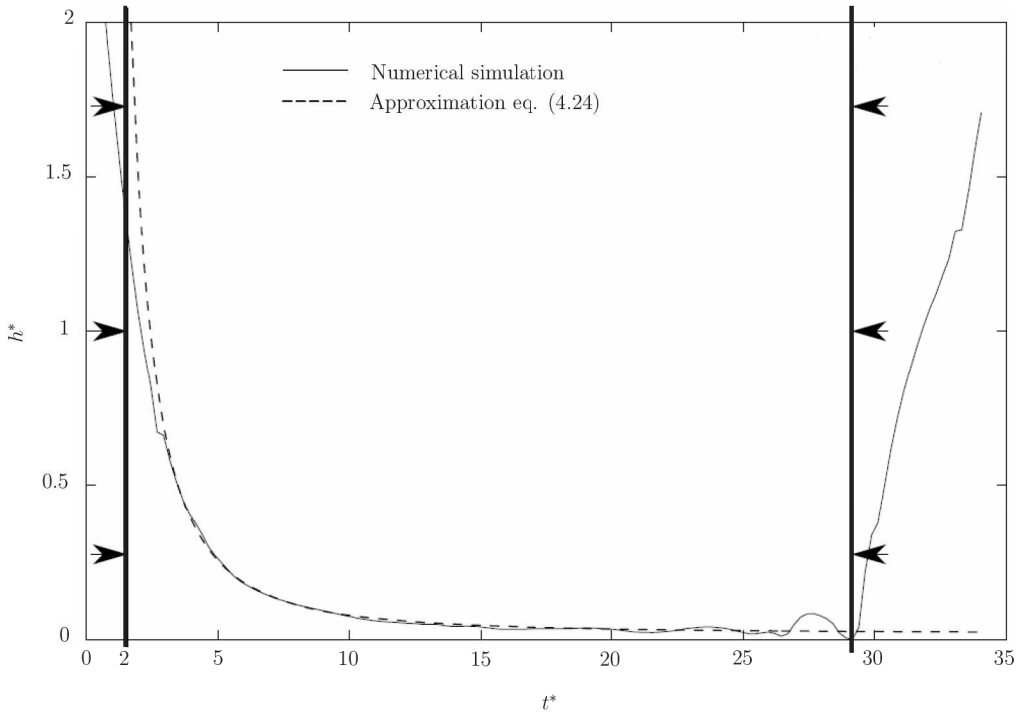

Figure 4.27: Boundary conditions for the approximation model of the minimum residual film thickness $h^*_{res,approx}$

4.5.2 Comparison between the numerical and theoretical residual film thickness

In §(4.5.1) a theoretical model has been derived for the minimum value of the residual film thickness during single drop impingement onto a steady liquid surface film. The general ex-

pression of this minimum residual film thickness is given by eq. (4.23), in which the value of the residual film thickness is a function of the Reynolds number only. In this paragraph the theoretical approximation will be compared with the numerical results, in order to validate the analytical model. Due to the limited spatial resolution of the camera with which the shadowgraph images were made (18.9 $\mu m/pix$) and the presence of the cavity reflections on the bottom of the plexiglass container, it is not possible to define the height of the minimum residual liquid film experimentally. Therefore the numerical results will be used as a comparison with the theoretical model.

Figure 4.28 shows the results of the numerical simulation of the single drop impingement for isopropanol onto two different initial surface film thicknesses $h^* = 1.0$ (left) and $h^* = 2.0$ (right) at different time instants. For both impingements the Weber and Reynolds number are kept the same. In these images blue corresponds to the gas phase ($\gamma = 0$) and red to the liquid phase ($\gamma = 1$).

Until a non-dimensional time $t^* = 2.0$ no difference can be observed between the shapes of the two cavities. For an initial film thickness of $h^* = 1.0$ a thin liquid film is formed at the bottom of the plexiglass for $t^* \geq 2$, of which its thickness goes asymptotically to a value larger than zero. At $t^* = 12$ the capillary wave, traveling downwards along the surface of the cavity, reaches the bottom of the liquid film and starts moving along the bottom of the liquid film towards the center of the cavity. From this time instant on the cavity recedes until the capillary wave has reached the center at $t^* = 18.5$. The evolution of the cavity for the impingement onto a liquid film of $h^* = 2.0$, however, shows a completely different behaviour. The receding phase, starting with the downward movement of the capillary wave, already begins during the time the cavity is still expanding in depth, see Figure 4.28(f) and 4.28(h). The capillary wave reaches the center of the cavity at the same time instant at which it also reaches the bottom of the liquid film, at about $t^* = 18.5$. For both impingements a central jet is seen to appear at $t^* = 21$, however, being much higher in the case of $h^* = 2.0$.

Although the influence of the bottom of the liquid film on the drop impingement process is only minor, the evolution of the cavity in time is completely different between both liquid films. The time evolution of the thickness of the liquid film, as well as the asymptotic minimum residual film thickness, can be approximated quite easily. Figure 4.29(a) and 4.29(b) show the evolution of the thickness of the liquid film in time after impingement for $h^* = 1.0$ and $h^* = 2.0$ respectively.

Looking at the evolution of the residual film thickness for $h^* = 2.0$ (Figure 4.29(b)) it is seen that until $t^* = 17$ the film thickness decreases steadily. For $t^* \geq 17$ the residual liquid film thickness increases again, leading to a very distinct minimum value of the residual liquid film thickness, usually found for drop impingement onto deep pools.

The curve of time evolution of the film thickness for $h^* = 1.0$ (Figure 4.29(a)) shows a steady decreasing motion until about $t^* = 17$. Between $t^* = 17$ and $t^* = 19$ an oscillation of the liquid film thickness is observed, which is growing in amplitude with time. These oscillations are the result of the combination of the downward motion of the capillary waves and the contraction of the cavity in radial direction, as has been explained above.

In §(4.5.1) a theoretical model has been derived with which the evolution of the film thickness in time during the expansion phase of the cavity can be approximated. With the use of eq. (4.24) the evolution of the thin residual liquid film below the cavity can be extrapolated at those time instants, at which the oscillations of the residual film thickness make it difficult to determine the absolute minimum residual liquid film thickness or at which the cavity has

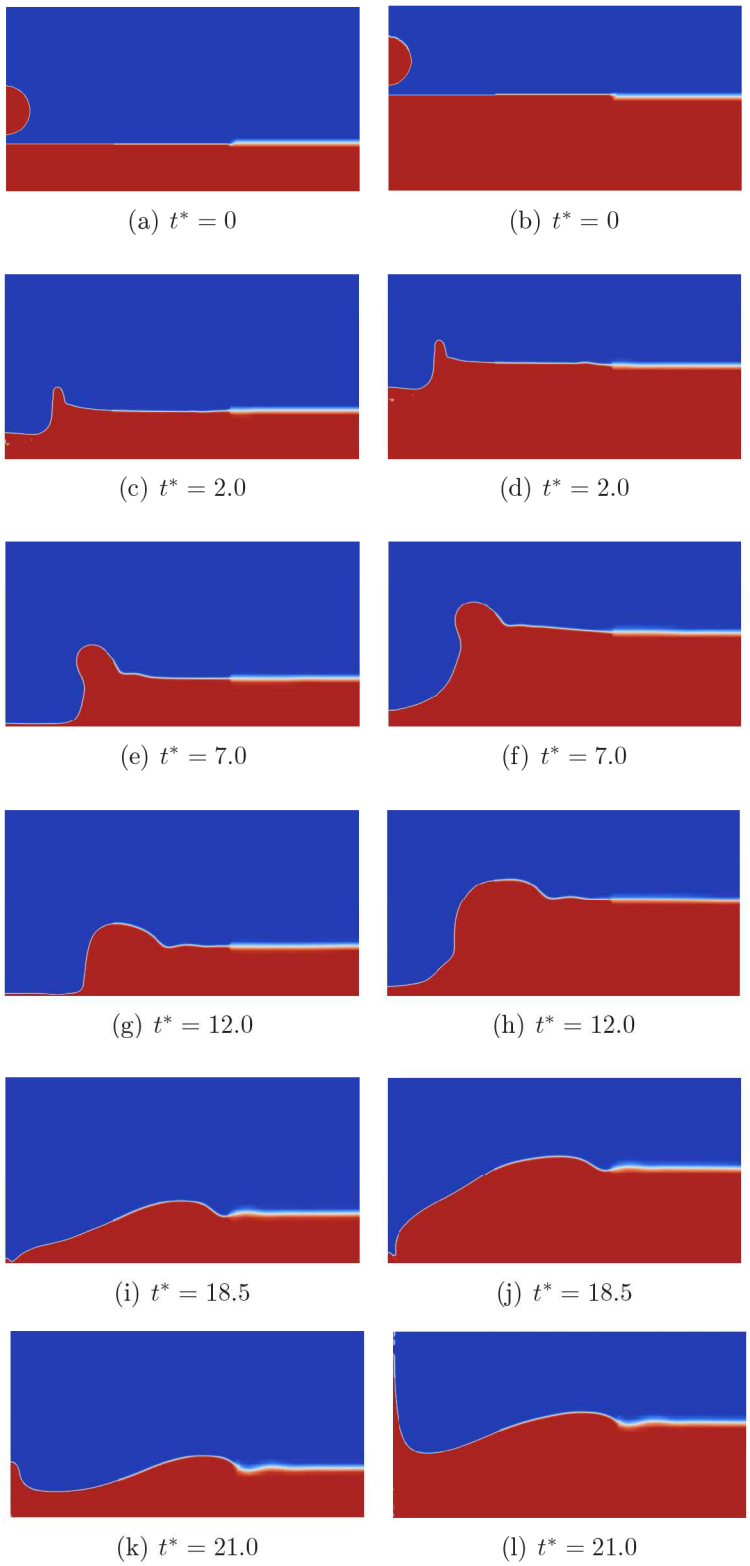

(a) $t^* = 0$ (b) $t^* = 0$

(c) $t^* = 2.0$ (d) $t^* = 2.0$

(e) $t^* = 7.0$ (f) $t^* = 7.0$

(g) $t^* = 12.0$ (h) $t^* = 12.0$

(i) $t^* = 18.5$ (j) $t^* = 18.5$

(k) $t^* = 21.0$ (l) $t^* = 21.0$

Figure 4.28: Numerical simulations of the single drop impingement onto a liquid layer of non-dimensional thickness: (left) $h^* = 1.0$, (right) $h^* = 2.0$. The evolution of the cavity formed by an isopropanol drop (left: $We = 192$, $Fr = 131$, $Re = 1,201$; right: $We = 189$, $Fr = 127$, $Re = 1,199$) impingement at various non-dimensional time instants

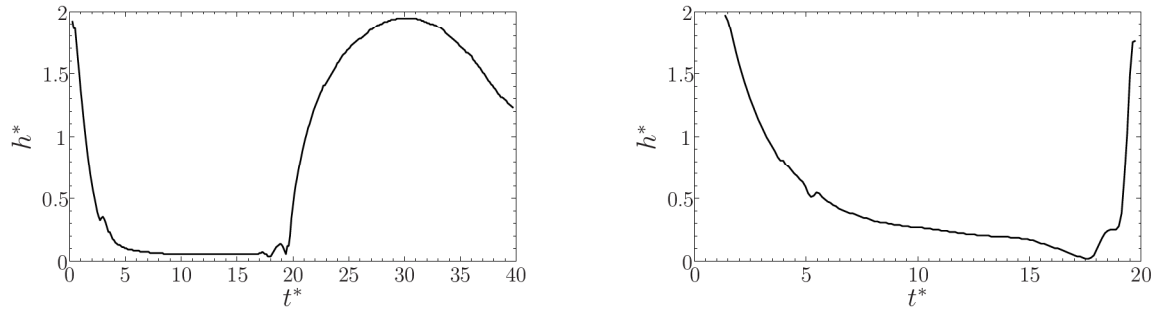

(a) $h^* = 1.0$ (b) $h^* = 2.0$

Figure 4.29: Evolution of the film thickness present below the cavity for $h^* = 1.0$ and $h^* = 2.0$. Comparison of the numerical results for the impingement of an isopropanol drop (a): $We = 192$, $Fr = 131$, $Re = 1,201$; (b): $We = 189$, $Fr = 127$, $Re = 1,199$

already started its retraction phase before the capillary waves have reached the center of the cavity. Since the approximation and the film thickness obtained by the numerical simulations converge asymptotically towards the residual film thickness, the absolute minimum residual film thickness can be obtained by $h^*_{res,approx} = c_3$ in eq. (4.24).

A comparison between the evolution of the film thickness based on the numerical simulations and those approximated by eq. (4.24) is shown in Figure 4.30 for several impingement cases. The curves are for different liquids, different Weber numbers and different initial film thicknesses, where it can be seen that the approximation for each of the simulated cases is very good. This means that the asymptotically obtained approximated values for the minimum residual liquid film thickness, obtained by $h^*_{res,approx} = c_3$ in eq. (4.24), are reliable. With the use of this approximation, the minimum residual liquid film thicknesses for all the simulated single drop impingements are obtained and listed in Table 4.3.

Table 4.3: Overview of the non-dimensional minimum residual liquid film thickness

			h^*				
Liquid	We_{mean}	Re_{mean}	**0.2**	**0.5**	**1.0**	**1.5**	**2.0**
Glycerine/water	479	539	0.064	0.071	0.084	0.099	0.105
Isopropanol	192	1,204	0.043	0.046	0.052	0.066	0.184
Isopropanol	536	2,002	0.039	0.040	0.048	0.058	0.088
Distilled water	110	4,670	0.029	0.030	0.029	0.062	0.253
Distilled water	337	8,491	0.021	0.023	0.021	0.034	0.076

In §(4.5) an analytical approximation has been derived to predict the minimum residual liquid film thickness, eq. (4.23), based on the remote asymptotic solution by Yarin and Weiss [196]. It has theoretically been shown that the residual film thickness correlates with $Re^{-2/5}$. The values of the minimum residual liquid film thickness, together with the analytical approximation are presented in the Figures 4.31(a) and 4.31(b). In the left figure the dependency of the minimum residual liquid film thickness on the Reynolds number of the impinging drop is